Wesleyan University The Honors College

Tracing the Evolution and Impact of the Stellar Winds of Solar-like Stars

by

Eric Edelman
Class of 2014

A thesis submitted to the
faculty of Wesleyan University
in partial fulfillment of the requirements for the
Degree of Master of Arts
with Departmental Honors in Astronomy

Middletown, Connecticut April, 2014

"Air, I should explain, becomes wind when it is agitated."

Titus Lucretius Carus

Acknowledgments

My sincere gratitude goes to NASA for their various forms of assistance with this project. I would like to acknowledge the NASA HST Grant GO-12475 awarded by the Space Telescope Science Institute, which is operated by the Association of Universities for Research in Astronomy, Inc., for NASA, under contract NAS 5-26555. Also, I must give my thanks for the student fellowship I was awarded from the Connecticut Space Grant Consortium in support of this research.

Certainly none of this work would have been possible without the continued support of the Wesleyan University Astronomy faculty and students, including my research and thesis advisor, Seth Redfield, who served as a consistent source of enthusiasm and wisdom through the entirety of this process. I must send out individual thanks to Stuart Flury for his wealth of advice on error analysis, Amy Steele for her knowledge of the less frequently encountered UNIX commands, and Dilovan Serindag for being the good Samaritan at the 11th hour.

Outside of Wesleyan, Brian Wood of the US Naval Observatory and Hans Müller of Dartmouth College made invaluable contributions towards the betterment and completion of this project. Also, I would like to send out the conventional yet sincere thank you to my family and friends, who have remained a consistent source of support and encouragement, without which I can hardly imagine how I would have managed to stay afloat.

Cheers, and many thanks.

Contents

Chapter 1

Introduction

When choosing a research project at Wesleyan University, I had the fairly common problem that novices in the field tend to share with children in candy stores. Frankly put, I needed to pick a single lollipop, while all the flavors in the universe seemed rather compelling. Although I have not covered the entirety of the universe in this thesis, I have gotten as close to that goal as I could manage, which is to say that I have remained remarkably distant from it. However, that initial, lighthearted desire is undoubtedly an ideal that has strongly influenced my choice of topic for research and the way I have approached it.

With an eye for the multidisciplinary and a newly passionate awe for and understanding of the incomprehensible vastness of the universe, I have studied objects in this thesis as distant as 18 parsecs away. Perhaps, when considering the above grandiose pontifications, one would think I should have tried to reach a little further outside of the solar system's astronomical backyard. In response, I feel that, in a way, I already have, in terms of the scope of the applications derived from the results within.

First, the initial focus of this project sweeps over absorption spectroscopy in terms of the gas between stars. The constraints derived from this investigation are then applied to modeling endeavors concerning stars like the Sun. These models are studied in terms of their potential effects on their orbiting planets'

atmospheres. Through a chain of intimately tied, admittedly local, phenomena, I go from the medium between stars, to the habitability of planets around them. The tie that links it all together is the stellar winds, and when introducing these winds I would consider it best to start at home.

1.1 The Solar Wind

The solar wind is a term that describes the "supersonic expansion of the corona," (Echim et al. 2011) and how those outflows continue onwards to interact with the gas and dust of interstellar space. There are a handful of instruments in space that focus on providing data concerning this wind. For example, NASA's *Solar and Heliospheric Observatory* (*SOHO*) has an instrument on board called the Charge, Element, and Isotope Analysis System, or CELIAS, that uses a charge sensor to discern the temperature and speed of the most common solar wind ions as they speed on by.[1]

Through careful observation and analysis, two distinct types of solar wind were uncovered: fast and slow. The fast winds come from holes in the corona, where the plasma density is lower than average, and leaves the Sun at speeds of approximately 750 km s^{-1}. The slow winds are mainly attributed to streamers, which are magnetic loops that form over active regions of the sun. True to their name, these slow winds are measured to be much slower than the fast winds, with an average speed of 400 km s^{-1}. However, their speeds are much more variable than those of the fast winds (Feldman et al. 2005).

The distribution of these two types of winds over time and location across the Sun is highly changeable, as shown by Figure 1.1. The 11 year solar cycle

[1]The CELIAS website: `http://www.space.unibe.ch/soho/instrument.html`

largely influences the proportion of coronal holes to streamers. Coronal holes dominate during solar minimum, and almost completely vanish during solar maximum. Streamers are inversely affected (Forsyth & Breen 2002).

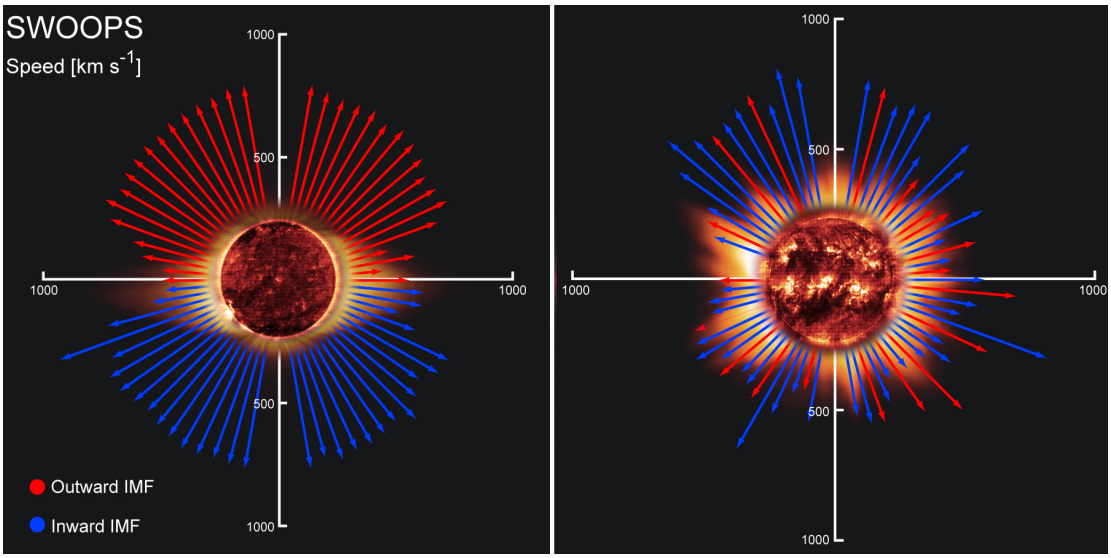

Figure 1.1: Solar wind variability as observed by *Ulysses* (ESA 2008). The arrows document the speeds of the winds moving off of the Sun at different latitudes. The left panel shows the wind speeds and the Interplanetary Magnetic Field (IMF) directions at solar minimum. The right panel shows how these variables change at solar maximum.

1.1.1 The Solar Wind Boundary

The solar wind does not travel forward indefinitely, but is eventually halted in its progression by the opposing force of the interstellar medium (ISM). The gas and dust flowing inwards towards the solar system and the hot plasma wind of the sun flowing outward towards the ISM eventually meet to form a boundary called the heliosphere.

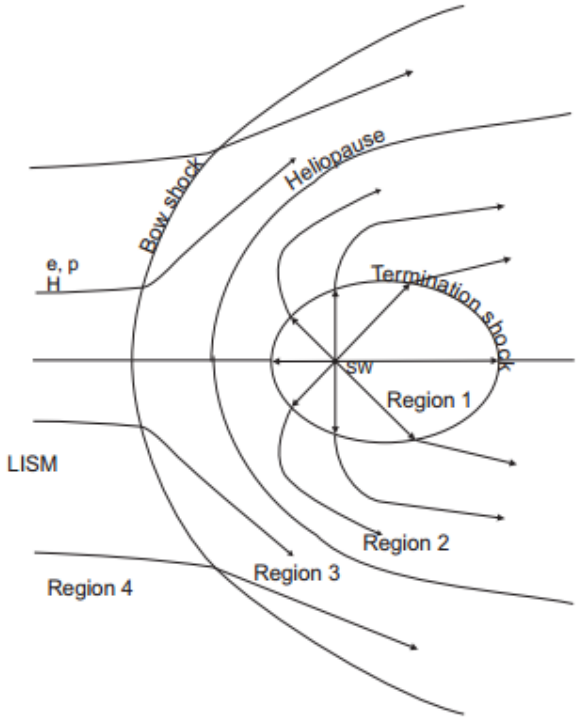

Figure 1.2: A diagram exemplifying the structure of the heliosphere from Izmodenov (2002). The solar winds (SW) are shown flowing outwards from the central SW point. They clash against the material of the LISM, or the local interstellar medium, flowing towards the solar winds on the left side of the image, forming the three-pronged structure of the heliosphere: the termination shock, the heliopause, and the bow shock.

Figure 1.2 provides a schematic of the structure of the heliosphere (Izmodenov 2002). Scientists have only been able to take in situ measurements of the heliosphere as early as 2003, thanks to the progress of the *Voyager* spacecrafts (Opher et al. 2006), where before only indirect measurements were possible through such methods as measuring plasma outflows from the Sun, as mentioned in Section 1.1.

The heliospheric structure can be divided into separate regions based on the level of interaction and speeds of the solar wind and the material from the interstellar medium. These parts will be considered here in order of increasing distance from the Sun.

First, there is the termination shock, where the winds of the Sun slow to

subsonic speeds. This region is considered to be situated out at a distance of 75-90 AU from the Sun and surrounds the entirety of Region 1 shown in Figure 1.2.

There is one section not shown in Figure 1.2 that lies between the termination shock and the heliosphere: the heliosheath. In this region, the solar wind becomes turbulent and continues to slow.

The next section of the heliosphere is the heliopause. This is the precise boundary where the winds of the Sun are expected to meet the material of the ISM, and is shown as the boundary between Regions 2 and 3 in Figure 1.2. The heliosphere has been adopted as a marker for determining *Voyager 1*'s transition from the inside to the outside of the solar system.

The difficulty in decisively knowing when a craft will cross this boundary comes with an extreme unfamiliarity with the conditions of that very boundary. The models produced to predict the physical characteristics of this region suffer from a lack of actual data from the regions themselves. With regards to the debate over *Voyager 1*'s progress through this section in particular, the expected response of the magnetic field to a crossing of the boundary was a high point of contention amongst the astronomical community. NASA first maintained the view that a change in the magnetic field should occur at the boundary, but changed their tune in September of 2013 when a coronal mass ejection from the Sun reached *Voyager 1* and provided new measurements of the surrounding plasma that convinced them otherwise (Gurnett et al. 2013).

When moving on to the final, outermost region of the heliosphere, it is first important to question whether or not the region actually exists. Astronomers debate whether or not the ISM flow relative to the Sun is strong enough to produce a bow shock, which would be the region where a supersonic ISM flow would

turn subsonic (McComas et al. 2012). While it is an uncertain feature in the heliosphere, most models do include it (Müller et al. (2008); Ben-Jaffel et al. (2013); Scherer & Fichtner (2014)). Figure 1.2 shows the bow shock as the division between Regions 3 and 4.

After the bow shock, if it does indeed exist, the heliosphere ends, and only the clouds of interstellar gas and dust of the local interstellar medium (LISM) remain. The ISM, particularly the LISM, shall be explored in further detail in Chapter 3.

1.2 The Winds of Other Stars

It is quite difficult to measure winds around other stars. We cannot place spacecraft directly in these stellar systems to measure plasma outflows; the only methods available are indirect, primarily selective towards detection of only the strongest nearby stellar winds, and are not universally applicable. Different stellar types have their winds most easily measured by different detection methods.

For example, stellar wind creates excess emission in the radio wavelengths through free-free or Bremsstrahlung emission caused through interaction between charged particles, which are plentiful in a stellar wind. However, the signal in the radio is quite small, so is only useful when detecting very strong winds (Lamers & Cassinelli 1999). Leitherer et al. (1997) used the *Australia Telescope Compact Array* to observe Wolf-Rayet stars at 8.64 and 4.60 GHz to determine mass loss rates, or stellar wind strengths for this type of star in the southern hemisphere out to distances of 3000 parsecs. Wolf-Rayet stars are extremely massive stars that were greater than 20 solar masses when on the main sequence, but have since evolved off and developed their notoriously strong winds, sloughing off material from the surface of the star to the tune of approximately $4 \times 10^{-5} M_{\odot}$ yr^{-1}. At

this rate, it would only take 25,000 years to lose mass of an entire Sun!

While the early type O and B stars, and post main sequence subgiants and giants were accumulating wind measurements, methods to detect the lower intensity winds of main sequence stars like the Sun have only emerged quite recently. Through a fantastic display of multidisciplinary collaboration, the method of detecting heliospheres through Lyman alpha (Lyα) absorption was created.

1.2.1 The Foundations of the Lyα Detection Method

In the 1990s, the *Hubble Space Telescope's* (*HST*) Goddard High Resolution Spectrograph (GHRS) was spearheading efforts to study the ISM in the ultraviolet, which included the Lyα transition at 1215.6700 Å. The GHRS took observations of the Lyα line toward nearby stars, so astronomers could model the absorption feature and constrain the properties of the intersecting ISM. However, attempts to fit this line were largely unsuccessful. The line appeared to be too broad when just considering the ISM absorption involved (Wood et al. 2004).

At the same time as groups were struggling with the Lyα inconsistency, other groups were expanding and updating models of the heliosphere. Most importantly in this context, the models were now "treating the interstellar neutrals and plasma in a self-consistent manner," (Wood et al. 2004) which hinted at the possibility of a heliospheric contribution to the Lyα absorption profile. A more technical, in depth discussion of this issue will be presented in Chapters 4 and 6, but for now, suffice it to say that the hydrogen in the ISM, as astronomers understood it at the time, was unable to account for all of the absorption found in the Lyα feature, and now there was another contributing factor they could consider when creating the profile.

Taking this line of consideration a step further, if solar winds can contribute to the Lyα profile can stellar winds make a similar contribution? Linsky & Wood (1996) discovered that yes, this was indeed a possibility, and made the first detection of an astrosphere - the heliospheric analogue around other stars - through use of the Lyα detection method on α Cen.

Through the combined efforts of surveyors of the ISM and modelers of the heliosphere, a new detection method to measure the stellar winds of solar-like stars was created. No other method to detect winds of stars like the Sun exists (Linsky et al. 2003), so it is an extremely singular and valuable tool when considering the properties of stellar systems like ours.

Chapter 2

Data

2.1 STIS *Hubble* Data

For this project, there are five target stars: HD9826, HD35296, HD72905, HD192310, and HD206860. The observations for HD35296, HD72905, and HD206860 come from Brian Wood's *Hubble* project proposal 12596, while HD9826 and HD192310 were observed under the auspices of Seth Redfield's *Hubble* project proposal 12475. Information about the target stars is listed explicitly in Table 2.1.

Line of sight spectral information to these five stars were obtained with use of the Space Telescope Imaging Spectrograph (STIS) on the *Hubble Space Telescope* (*HST*) with echelle spectroscopy, a technique first considered by Michelson (1898).

Echelle is French for the word ladder, and, true to its name, presents many 'rungs' of spectra, as shown by the upcoming Figure 2.1. This two dimensional

Table 2.1: Target Star Information.

Object Name	Distance (pc)	l (deg)	b (deg)	Type	V (mag)	V_R (km s^{-1})	Known Planets
HD9826	13.49 ±0.03	+132.0	−20.7	F9V	4.1	−28.59 ±0.08	4
HD35296	14.39 ±0.08	+187.2	−10.3	F8V	5.0	+37.70 ±0.20	0
HD72905	14.36 ±0.08	+150.6	+35.7	G1V	5.6	-13.03 ±0.12	0
HD192310	8.91 ±0.02	+015.6	−29.4	K2V	5.7	−54.2 ±0.90	2
HD206860	17.90 ±0.14	+069.9	−28.3	G0V	6.0	−16.68 ±0.09	1

Information regarding the distance, coordinates, spectral type, magnitude, and velocity was taken from the simbad database.

layout is one of the unique flavors of the echelle spectroscopy technique that is necessitated by the peculiarity of its diffraction grating. A diffraction grating diffracts different wavelengths of light in particular directions, and one of its defining characteristics is the spacing between the slits or ridges it uses to diffract the light. For echelle spectroscopy, these ridges are distinctively far apart from each other, which causes a great deal of dispersion of the light, which would mean overlap of different wavelengths on the end spectral product if not for a second grating or prism that then splits the light perpendicular to its original split, a technique known as cross dispersion. The end product then has rows - or rungs - of spectra (Porter 2000).

The MgII lines at 2796.3553 Å and 2803.5324 Å, and the FeII lines at 2586.6500 Å and 2600.1729 Å were observed with the STIS grating E230H, which encompasses the wavelengths of 1620-3150 Å at a high resolving power of 114000. The deuterium (DI) at 1215.3376 Å and 1215.3430 Å, and the HI Lyα at 1215.6682 Å and 1215.6736 Å were observed with the STIS grating E140M, which encompasses the wavelengths of 1144-1729 Å at a medium resolution of 45800 (Hernandez 2011). The resolution of a spectra indicates how close two objects can be in wavelength space and still be discerned as two unique objects, as shown by Equation 2.1.

$$R = \frac{\lambda}{\Delta\lambda} \tag{2.1}$$

The denominator is the resolution limit, while the numerator is the wavelength under use. As the wavelength decreases, smaller $\Delta\lambda$ become possible for the same resolution, and, as the wavelength increases, the size of the $\Delta\lambda$ limit decreases in tandem. A lower resolution is acceptable when analyzing Lyα and DI, because the lines are much broader than the MgII and FeII lines and at lower wavelengths. For

example, in the HD192310 data the MgII 2796 Å emission feature is approximately 1.1 Å wide, while the Lyα emission feature is just about twice as wide. Figure 2.1 provides an example of what the E230H high resolution raw data looks like before reduction, with particular emphasis placed on the positions of the MgII lines visible in the spectrum.

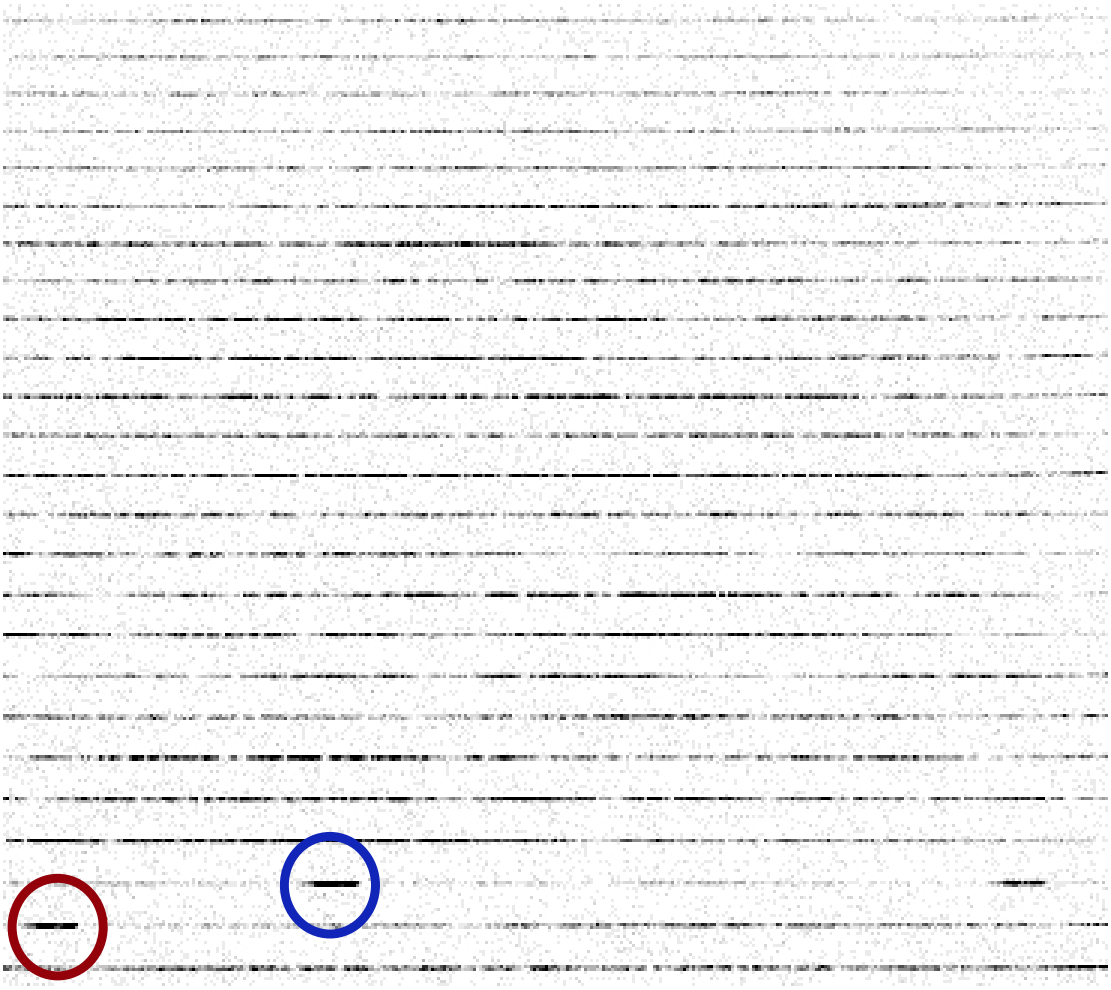

Figure 2.1: This is the high resolution portion of the raw data received from the STIS for target HD192310. A diffraction grating centered at 2713 Å was used to separate the wavelengths. The amount of black equates to the intensity received at each respective wavelength. Two significant features are circled near the bottom of the figure. In blue, the MgII 2796 Å line is shown. The MgII 2803 Å line is circled in red. The image has been modified to emphasize the variation in intensities.

The data reduction process was completed with a *Hubble*-specific data reduction software package known as `CALSTIS` (Redfield & Linsky 2001), enhanced by StarCAT (Ayres 2010). This program takes care of all the standard reduction tasks for a 2-D image, such as overscan and dark subtraction.

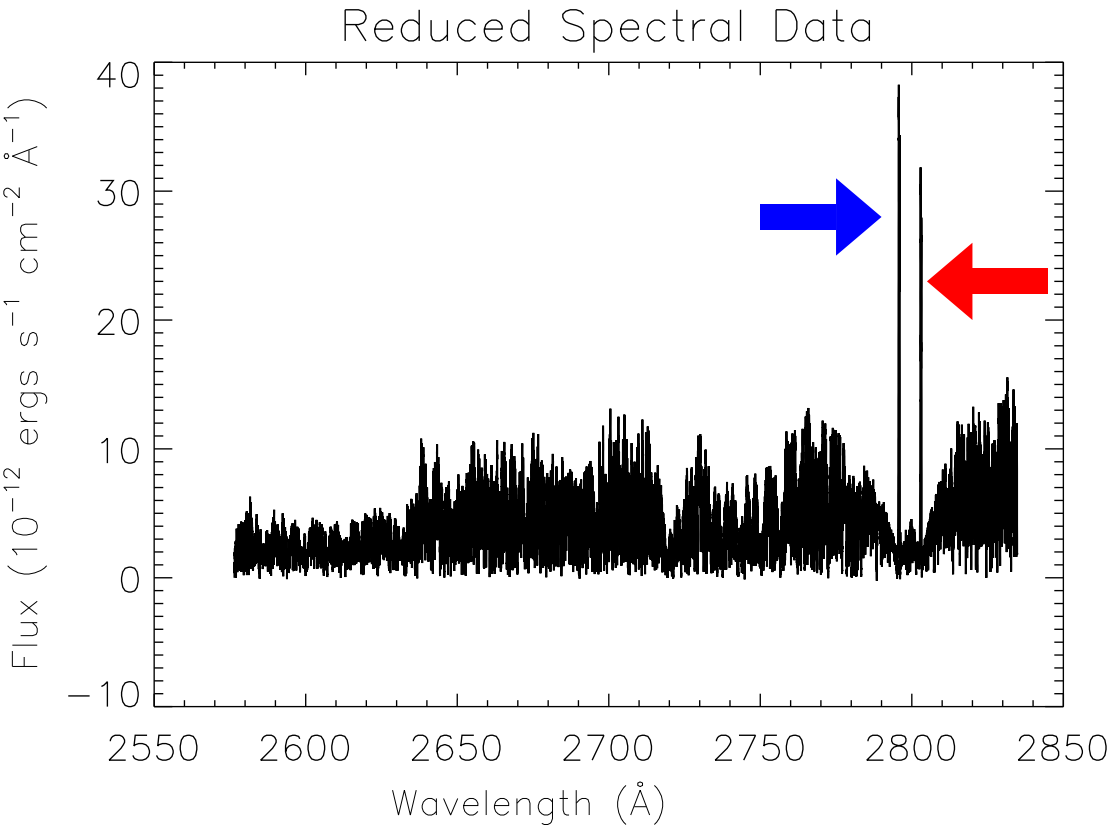

Figure 2.2: This is the same spectrum shown in Figure 2.1 now post data reduction. The blue and red arrows point to the MgII 2793 Å and 2803 Å lines respectively, just like the circles in Figure 3.1.

An overscan subtraction uses virtual pixels to subtract the electronic bias of the image. Virtual pixels are created by forcing the CCD readout to go past the limit of physical pixels in a row. For example, with an image that has physical data for 1024 x 1024 pixels, an overscan can create a frame of 1062 x 1024 pixels. With these extra pixels, an average electronic bias level is created and subtracted for each line of the image using the program `BLEVCORR` (Hernandez 2011).

To get rid of dark current in the image, dark frames are used. With STIS, one super dark frame made of around 50 individual darks with exposures more than 900 seconds is used for the subtraction. The `DARKCORR` program in `CALSTIS` is used for this portion of the reduction (Hernandez 2011).

Quite a few other tasks are performed, such as flat field calibration, flux unit and Heliocentric rest frame conversions, wavelength calibrations, and 2-D to 1-D spectrum extraction (Hernandez 2011). At the end of the reduction pipeline, the image comes out looking like Figure 2.2. It is now a 1-D image of spectra across a wavelength range in Å and a flux range in cgs units.

2.2 Primary Programs

There were two primary programs used to fit ISM absorption features in the data, with both programs created by Seth Redfield.

2.2.1 `MKFB`

`MKFB` is a program written in IDL that is used to reconstruct what the continuum most likely looked like before any absorption occurred, which is a process that is explained in more detail in Section 3.2. This program provides multiple ways to reconstruct the continuum that vary in efficacy depending on the individual characteristics of the line in question. `MKFB` fitting methods of particular usefulness for this project were the polynomial fit method and the continuum reversal methods.

The polynomial fit method creates a polynomial of the user-specified order between 1 and 10 that best connects together two or more user-specified regions of flux. This method is usually the best performer when line symmetry is not

overly prevalent. An example of this is shown in Figure 2.3. The MgII emission feature in the figure lacks symmetry in its two peaks, with one peak significantly higher than the other, so the continuum reversal method could not be used in this case.

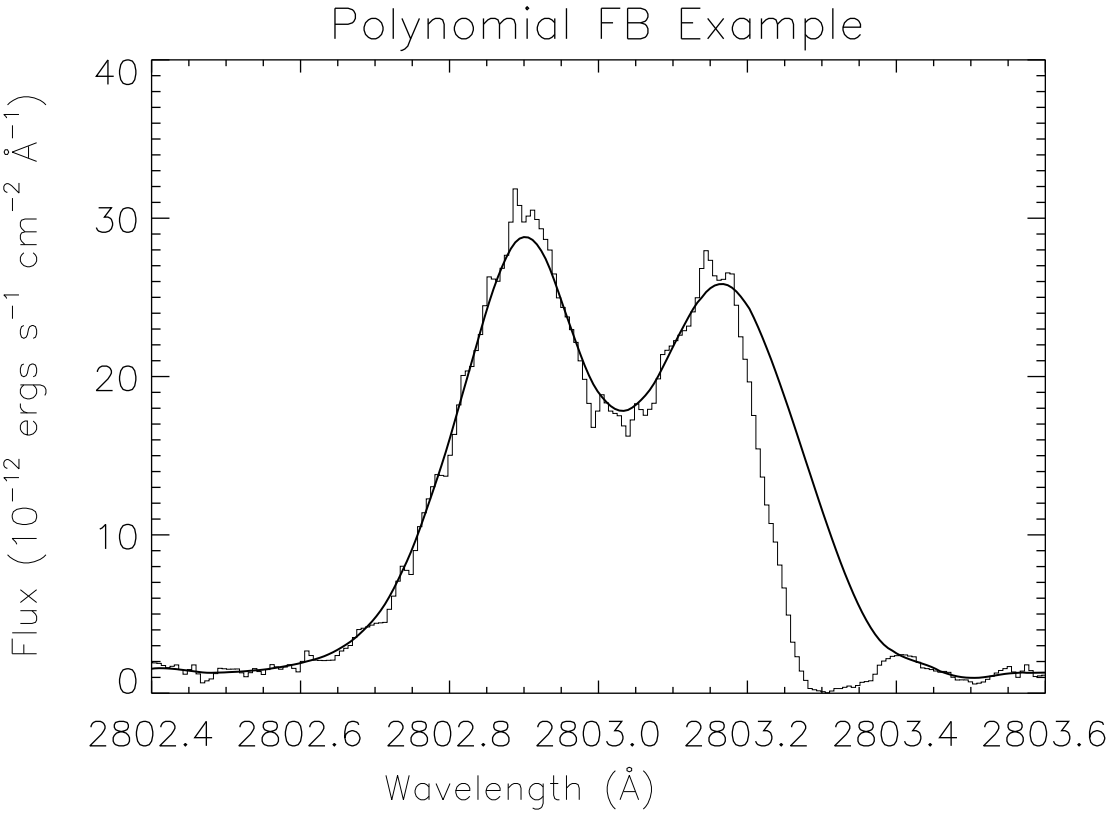

Figure 2.3: Here is an example of a continuum reconstructed for the MgII 2803 Å line from HD192310 with the polynomial fit method. The solid line is the reconstructed continuum, while the histogram is the untampered received flux. The program only develops a polynomial for the portion of the flux over the absorption feature, shown as the portion of the feature where the solid line greatly diverges from the histogram. The reconstructed continuum along the rest of the emission feature is simply an average and smoothed value of the received flux.

However, if there is significant emission feature symmetry, then flipping the profile of the line can be an effective alternative. This technique involves flipping the continuum and fitting the appropriate part of the flipped continuum into the gap created in the flux by the absorption feature, and an example of such is shown

in Figure 2.4. For emission features that exhibit Gaussian-like symmetry, or a central reversal with two symmetric peaks, such as with Figure 2.4, this technique can produce an extremely close representation of the disrupted continuum.

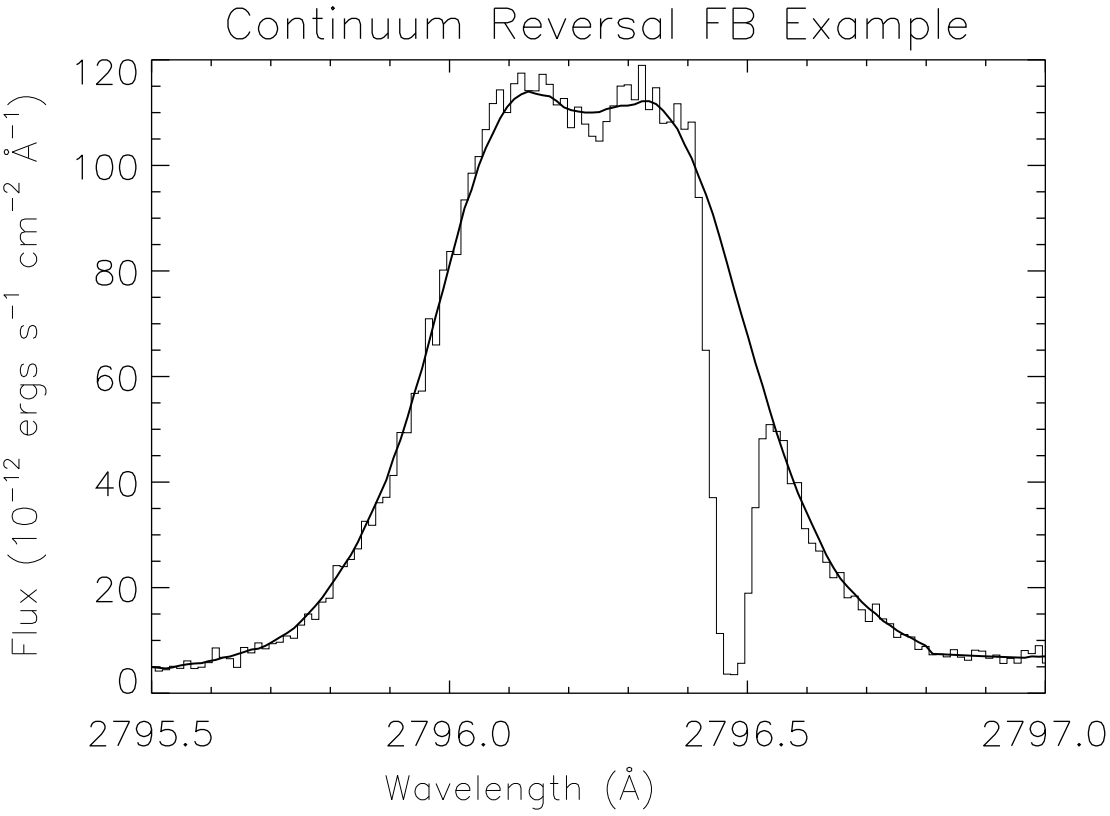

Figure 2.4: Here is a continuum reconstructed for the MgII 2796 Å line from HD72905 through the continuum reversal method. The solid line is the reconstructed continuum, while the histogram is the untampered received flux. This emission feature has two very symmetric peaks, so using the smooth, uninterrupted continuum to cover the absorption dip on the right side of the feature works well to reconstruct the line.

2.2.2 `GISMFIT`

`GISMFIT` is a program written in IDL that is used to estimate the Gaussian parameters of the absorption features present. The program uses inputs for the atomic parameters of each particular elemental transition taken from Morton (2004), as well as user input estimations for the Gaussian parameters of each

absorption feature: Doppler velocity, b value, and column density. These three parameters will be explained in detail in Section 3.1.

With all of these inputs, as well as the reduced data from STIS containing information regarding the flux and error per wavelength, the program returns best fit values for each component of absorption. The errors for each parameter are computed through Monte Carlo iterations that contribute towards a reduced χ^2 (Chi-squared) value.

Many iterations of a Monte Carlo calculation is a way of determining the uncertainty of a produced fit of a function. How sensitive is the fit to subtle, or even large changes in the input parameters? How well does the fit match the data being fitted? The Monte Carlo simulation provides randomly generated alternative inputs to see how well the fit performs under such variations (Lemieux 2009). In the case of this project, almost all fits are supplemented with 100 iterations of the Monte Carlo calculation to substantiate the χ^2 calculation.

At its simplest, the χ^2 equation can be written as:

$$\chi^2 = \sum \frac{(O-E)^2}{E} \tag{2.2}$$

As Equation 2.2 exemplifies, the χ^2 value is the summation of the square of the observed values (O) minus the expected values (E) divided by the expected value. This gives a measure of the deviation of the computed function over the entire domain being considered. If the O's deviate wildly and frequently from E's then the χ^2 will be large, indicating a bad fit. Instead the ideal is to have the observed values be as close to the expected values as possible, bringing the χ^2 value down close to 1.

For the problem of fitting absorption features, the calculation of the χ^2 is not

quite as simple as applying the above equation to the data. The fit parameters associated with the minimum χ^2 value for this project are calculated through the Levenberg-Marquardt least squares fitting method. This is a way of finding the minimum χ^2 for a function that has multiple parameters to be fitted that are not related linearly. Deviations from the expected value for one parameter may need to be weighted more heavily than deviations of another parameter (Quinten 2012).

There are at least three parameters to be fit for each absorption feature calculation. To understand just what these parameters are and what they mean in the context of a calculation of the strength and shape of an absorption feature, it is important to have a basic understanding of the clouds they come from.

Chapter 3

The Interstellar Medium

Between us and the stellar systems of nearby stars there is much more than simply empty space. An entangled network of interstellar clouds of gas and dust surround and interact with the local stellar neighborhood.

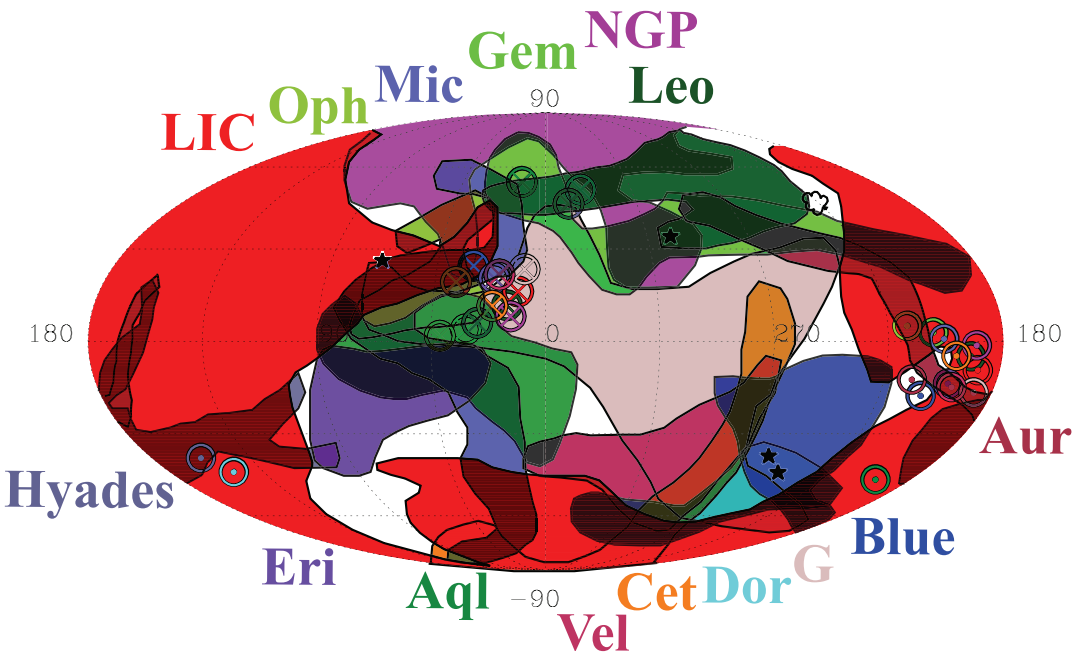

Figure 3.1: This is an up to date map of the local interstellar medium with positions in galactic coordinates, and morphologies for identified nearby clouds from Redfield & Linsky (2008).

As shown in Figure 3.1, the LISM is a complex environment filled with a variety of interstellar clouds. When analyzing line of sight spectroscopic information to stars through these clouds, their influence upon the data must be taken into

account. One way this can be accomplished is through careful scrutiny of the absorption features of specific elemental transitions that can be attributed to the ISM, such as AlII, FeII, HI, MgII, OI, and SiII to name only a few (Redfield & Linsky (2002); Redfield & Linsky (2004a)). Because of the wavelength ranges provided through the data received from STIS, this project focuses upon absorption features present in FeII, MgII, DI, and, of course, HI Lyα. This chapter will focus only upon MgII and FeII, because they are absorption features that come solely from the interstellar medium. They are heavy, narrow ions, which provide an excellent opportunity to investigate the compact structure of the ISM along the line of sight. While the DI absorption feature is also purely ISM, its intimate ties to Lyα find the line more suited for analysis and description within the fourth chapter.

3.1 An Overview of ISM Absorption

When fitting for absorption features of the ISM, the two most important ions evident in the spectral range of data covered by the STIS are MgII and FeII, with absorption lines positioned at 2796 Å and 2803 Å, and at 2586 Å and 2600 Å respectively. Each ion has two individual lines, providing four unique opportunities to potentially detect and analyze ISM absorption.

One can discern an absorption feature as a dip below the regular emission for a particular line, such as the noticeable valley visible in HD72905's continuum at 13 km s^{-1} shown in Figure 3.2. This simple dip is full of information about the number and physical parameters of the clouds along the line of sight between the Sun and the target star.

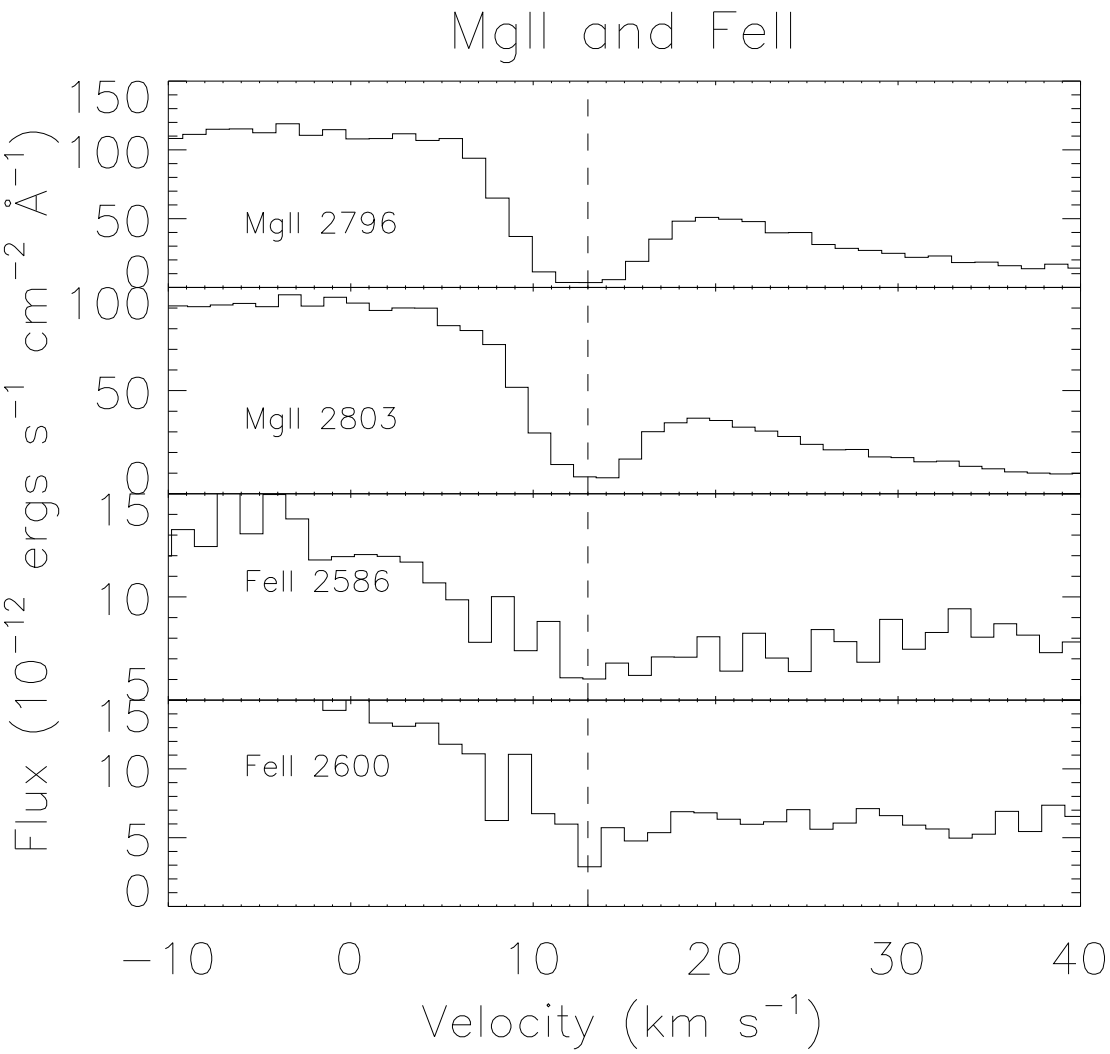

Figure 3.2: This figure shows the four aforementioned emission lines for MgII and FeII for the target HD72905. The x-axis is in heliocentric radial velocity space, with the absorption feature at 13 km s^{-1}, shown by the dashed vertical line.

Each individual cloud contributes absorption to the line in the form of a Voigt profile, of which its Gaussian parameters provide information on the radial velocity of the cloud relative to the Sun, the Doppler width of the line, and its column density. In terms of a Gaussian function:

$$f(x) = a * e^{-(x-b)^2/2*c^2} \tag{3.1}$$

where b is the offset of the center of the peak from zero, c dictates the width of the curve, and a equals the amplitude of the Gaussian, b is the velocity parameter, c is related to the Doppler Width, and a translates to the column density parameter.

The velocity value measures the movement of the cloud in the radial direction along the line of sight. If the cloud is moving toward the Sun, the velocity will be blueshifted, and the feature will be identified at a wavelength smaller than the known central line wavelength. This would translate into a negative velocity in Figure 3.2. Movement away from the Sun would translate into a redshift and a positive velocity, as identified for the feature in HD72905's line of sight data.

Because the absorption for features for both lines of MgII and FeII are created by the same cloud or clouds along the line of sight, they will all be positioned in the same place in velocity space relative to each other, which is a consistency that is useful when attempting to accurately fit the Voigt profile and measure different Gaussian parameters of each absorption feature. Each individual fit of an absorption feature can serve as a check on the accuracy or lack thereof of any other.

The Doppler width, also known as the b value, is a quantity that describes the radial velocity dispersion of a particular ion along a line of sight:

$$b^2 = \frac{2kT}{m} + \xi^2 \tag{3.2}$$

Equation 3.2 shows how Doppler width is dependent on both thermal broadening and non-thermal, or turbulent, processes, with k as the Boltzmann constant, T defined as temperature, m as the mass of the ion, and ξ defined as the turbulent velocity of the gas in question.

For most of the ISM absorption of the heavier ions such as MgII and FeII,

turbulent processes will be the dominating contributor. Since m is in the denominator of the thermal component of Equation 3.2, the larger the mass, the higher the temperature T required to make the thermal term significant. A recent survey done by Redfield & Linsky (2004b) found the mean temperature of LISM to be 6680 $\pm$1490 K within 100 parsecs of the Sun. These ISM clouds under consideration are not warm enough for thermal influences to have a large effect on the width of absorption features of heavier ions such as FeII and MgII, although MgII will often be detected to have a slightly larger Doppler width than FeII because of its lighter mass. The affect on the DI and Lyα transitions, which both involve the lightest element, hydrogen, is much more significant, and thus thermal broadening will play a much more dominant role in the fits discussed in Chapter 4.

The column density is the density of the particular ion along the line of sight, or column. An ISM cloud with a higher abundance of a certain ion relative to another cloud will have a deeper absorption feature for the ion in question. Also, lines of sight that travel further into clouds than others will see higher column densities. Extremely high column densities can even lead to line saturation (see Section 3.3.3). Smaller abundances lead to weaker absorption features, and minimal to nonexistent abundances mean that there will be no hint of visible absorption in the data.

These abundances may vary from ion to ion, as well as from cloud to cloud. For example, each ion being considered will cover a unique percentage of its element's ionization distribution. For FeII this percentage is greater than 95%, while for DI and MgII this percentage is between 55% and 85% (Redfield & Linsky 2004b). Also, dust grains can be destroyed through phenomenon such as supernova shocks, which can vary abundances on a cloud to cloud basis (Redfield & Linsky 2001). Another issue than can affect cloud to cloud abundances is depletion into dust

grains. Some elements in a cloud may "condense into solid form," (Jenkins 2014) depleting the amount of gas to be measured.

3.2 The Fitting Process

In order to use the three Gaussian parameters to fit for absorption, first it is important to know how much absorption to fit. This is accomplished through reconstruction of the part of the continuum of the line that was destroyed in the process of absorption.

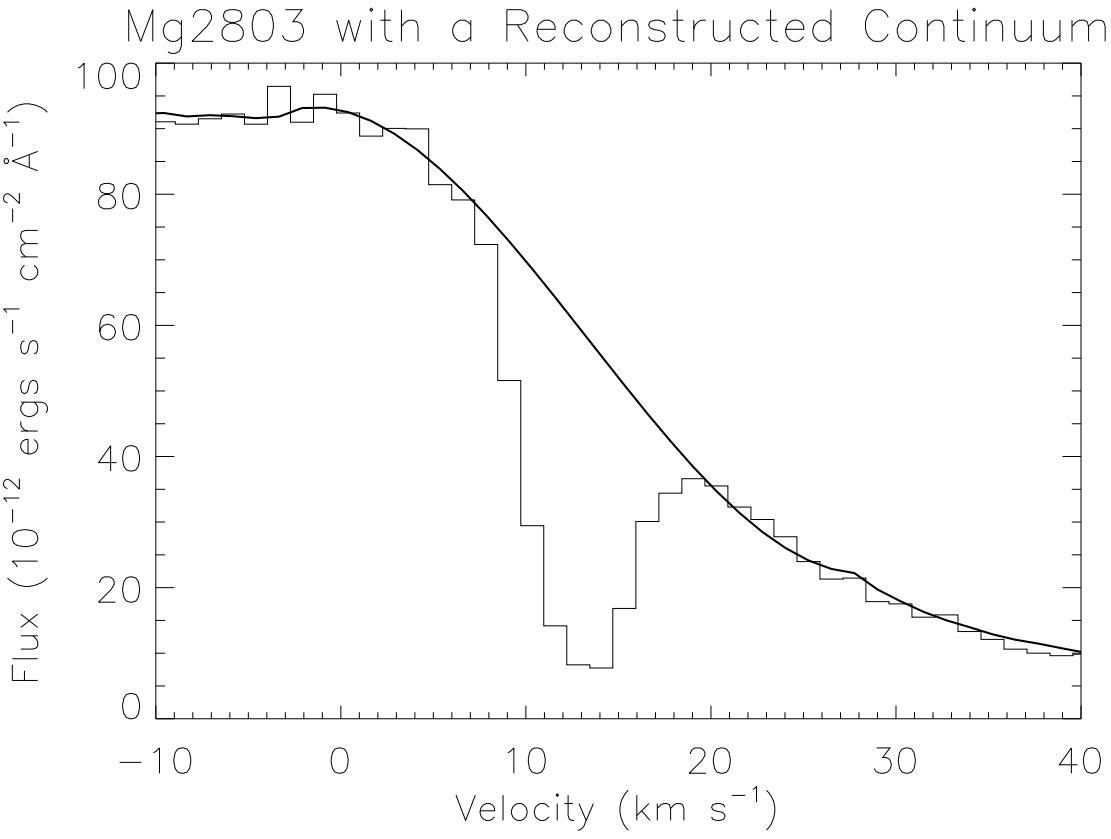

Figure 3.3: This figure is focused upon the 2803 MgII line from the HD72905 data, which is the second feature from the top in Figure 3.2. The reconstructed continuum is superimposed on the figure as a solid black line. The original continuum shape is signified by the histogram.

This process is completed through careful consideration of the normal shape

of the continuum outside of the absorption feature and through reference to what the unabsorbed emission features of different ions should look like per stellar type. Reference continua can be found in such works as Redfield & Linsky (2002) and Wood et al. (2000). With this knowledge, `MKFB` (See Chapter 2) is used to construct a model continuum, like the one shown in Figure 3.3.

Now, with a proper continuum, a fit of the absorption feature or features can be attempted through use of the `GISMFIT` program (See Chapter 2). First, a user inputs the appropriate atomic parameters unique to each ion, which include the central wavelength (λ), the natural broadening coefficient (γ) and the oscillator strength (f). λ can be calculated through knowledge of the two different energy levels involved in the transition, as shown through the formula supplied by Morton (2004):

$$\lambda_{lu} = \frac{10^8}{(E_u - E_l)} \tag{3.3}$$

Equation 3.3 solves for the wavelength for a transition between a lower energy state E_l and an upper energy state E_l. γ takes into account the quantum mechanical uncertainties of the line that broaden it from this central wavelength without considering the possibilities of thermal or turbulent influences. The formula for γ is as follows:

$$\gamma_{ul} = \frac{1}{\tau_u} + \frac{1}{\tau_l} \tag{3.4}$$

In Equation 3.4, τ is the lifetime of the upper (τ_u) and lower (τ_l) energy levels associated with the transition in question. A transition with a naturally shorter lifetime will have a larger γ, and thus have larger natural broadening (Morton 2004).

The final input, f, is a measurement of the strength of the transition, with the basis of comparison being "a classical, single electron oscillator" (Hilborn 2002).

After the atomic inputs, the user directs the program to the line spread function (LSF) to be used, such as the ones shown in Figure 3.4. The LSF takes into account the systematic blurring of the image and can be measured by the full width at half max (FWHM) of the function, with smaller numbers indicating less blur or spread of pixels (Hernandez 2011).

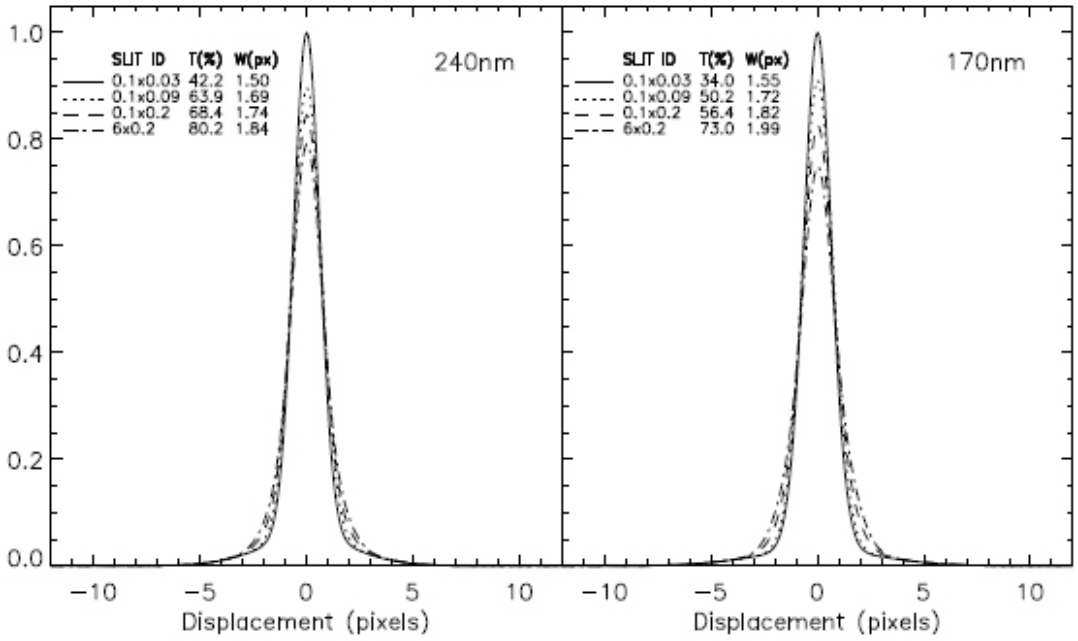

Figure 3.4: This is a figure from Hernandez (2011) representing LSF for E230H spectra, which include the MgII and FeII lines. The broader the line is, the worse the systematic blurring of the device will be, as more pixels fall outside of the expected area. The function on the left is the LSF for objects at 2400 Å, while the function to the right is the LSF for objects at 1700 Å.

When all of the aforementioned inputs are taken care of, the `GISMFIT` program will take guesses for the three Gaussian parameters of amplitude, width, and center offset, and comes up with a best fit Voigt profile for each absorption component, considering the errors associated with the data and minimizing the χ^2 value for the

fit. Figure 3.5 shows one such fit for HD72905's MgII 2803 line. The ISM values obtained from fits of ISM absorption components for all of the stars considered in this thesis can be found in Table 3.1.

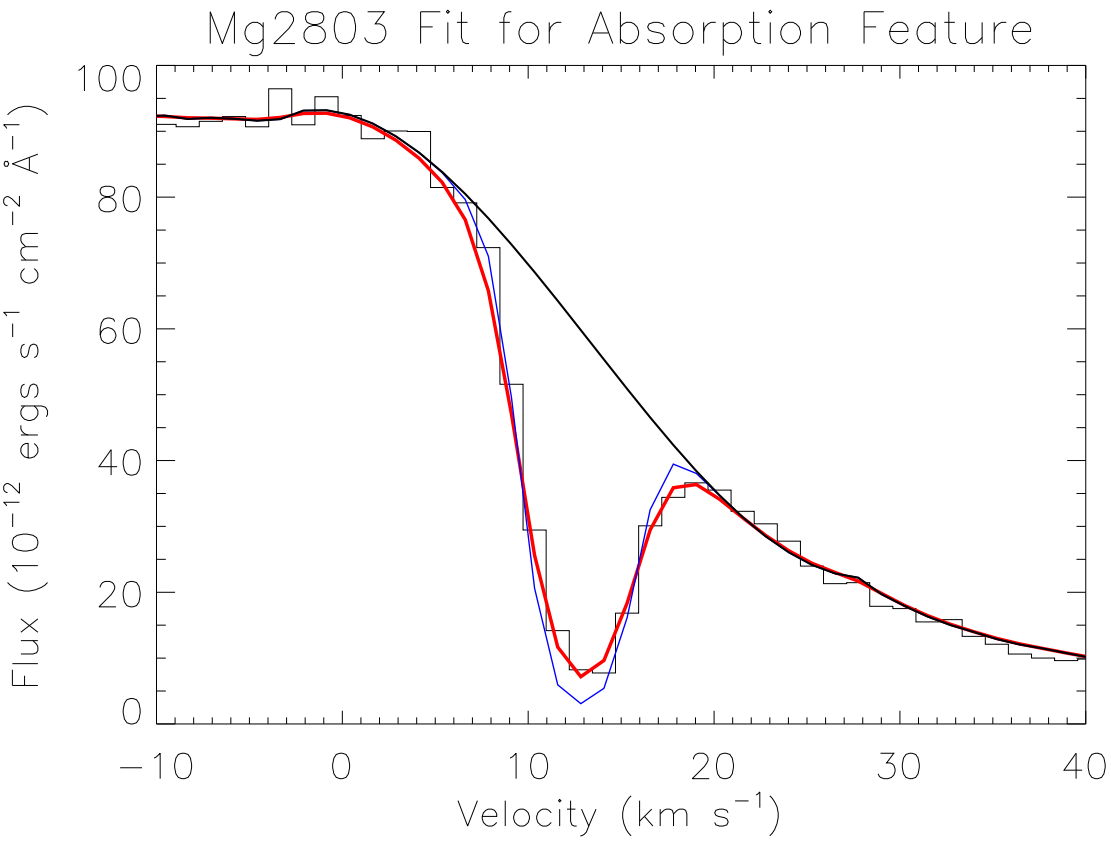

Figure 3.5: This is a fit of the absorption feature for HD72905's MgII 2803 line. The individual absorption component is shown as the thinner blue line, which, when convolved with the LSF for this wavelength regime, produces the total absorption. The total absorption for this feature is shown as the thick red line, which adheres strongly to the unaltered continuum, as is the expectation and goal. The reconstructed continuum is the thick black line, that diverges from the histogram continuum only above the absorption feature, just like Figure 3.3.

3.2.1 Simultaneous Fits

Fitting an absorption feature of a single line for a single ion is a process layered with uncertainties. Such questions as 'Is my reconstructed continuum an accurate

Table 3.1: ISM Fit Parameters.

Object Name	Comp. Number	Ion	Radial Velocity (km s^{-1})	Doppler Width (km s^{-1})	Column Density (log cm^{-2})	SNR
HD9826	1	FeII	10.94 ± 1.84	3.38 ± 0.63	11.92 ± 0.11	21.1
	1	MgII	8.05 ± 0.72	2.02 ± 0.29	11.57 ± 0.13	28.2
	1	DI	10.05 ± 0.90	7.17 ± 1.30	12.69 ± 0.18	19.8
	2	FeII	12.35 ± 0.86	2.56 ± 1.07	12.19 ± 0.06	21.1
	2	MgII	12.04 ± 0.16	2.40 ± 0.37	12.49 ± 0.05	28.2
	2	DI	14.33 ± 0.90	6.73 ± 1.50	12.88 ± 0.16	19.8
	3	FeII	16.67 ± 0.79	2.04 ± 0.71	12.02 ± 0.09	21.1
	3	MgII	16.30 ± 0.21	2.47 ± 0.17	12.38 ± 0.05	28.2
	3	DI	18.24 ± 0.90	8.78 ± 1.86	12.70 ± 0.16	19.8
HD35296	1	FeII	19.55 ± 0.31	0.77 ± 0.56	11.69 ± 0.10	14.9
	1	MgII	19.39 ± 0.42	1.75 ± 0.46	$11.51^{+0.24}_{-0.55}$	37.4
	1	DI	17.96 ± 0.71	5.2 ± 2.0	12.44 ± 0.22	20.2
	2	FeII	23.83 ± 0.31	0.63 ± 0.34	$11.83^{+0.20}_{-0.39}$	14.9
	2	MgII	23.61 ± 0.12	2.15 ± 0.18	12.34 ± 0.03	37.4
	2	DI	22.17 ± 0.71	5.0 ± 1.3	12.80 ± 0.14	20.2
HD72905	1	FeII	13.36 ± 0.33	1.43 ± 0.63	12.23 ± 0.10	12.5
	1	MgII	12.83 ± 0.16	2.53 ± 0.08	12.78 ± 0.01	38.7
	1	DI	11.86 ± 0.19	6.47 ± 0.27	13.21 ± 0.02	24.4
HD192310	1	FeII	-30.69 ± 0.66	4.02 ± 0.72	12.57 ± 0.07	5.4
	1	MgII	-31.07 ± 1.50	3.73 ± 0.82	12.20 ± 0.09	18.2
	1	DI	-30.34 ± 1.03	6.98 ± 1.32	12.85 ± 0.20	12.6
	2	FeII	-24.04 ± 0.51	2.53 ± 0.64	12.57 ± 0.11	5.4
	2	MgII	-24.46 ± 0.55	3.76 ± 0.60	13.20 ± 0.13	18.2
	2	DI	-24.89 ± 1.03	7.67 ± 1.05	13.01 ± 0.13	12.6
	3	FeII	-19.02 ± 2.10	2.48 ± 1.87	12.10 ± 0.16	5.4
	3	MgII	-18.88 ± 1.38	2.44 ± 0.76	12.46 ± 0.21	18.2
	3	DI	-19.02 ± 1.03	6.55 ± 1.44	12.73 ± 0.23	12.6
HD206860	1	FeII	-13.80 ± 0.98	2.35 ± 0.71	11.99 ± 0.09	11.4
	1	MgII	-14.77 ± 0.41	2.59 ± 0.17	12.67 ± 0.04	30.3
	1	DI	-14.84 ± 0.67	9.72 ± 1.56	13.05 ± 0.13	10.4
	2	FeII	-7.14 ± 0.91	2.47 ± 0.39	12.69 ± 0.12	11.4
	2	MgII	-7.43 ± 0.69	3.47 ± 0.27	13.22 ± 0.28	30.3
	2	DI	-9.00 ± 0.67	7.13 ± 1.91	13.19 ± 0.38	10.4
	3	FeII	-5.00 ± 0.65	2.11 ± 0.51	12.89 ± 0.08	11.4
	3	MgII	-4.87 ± 0.82	2.07 ± 0.30	14.16 ± 0.20	30.3
	3	DI	-6.29 ± 0.67	6.48 ± 1.51	13.31 ± 0.23	10.4

representation of the actual continuum?' and 'There are a few fits that work really well for this absorption feature, but which one best represents the actual ISM absorption?' arise. One strategy to emolliate some of these worries is to do a simultaneous fit.

This is the process of fitting two separate lines associated with the same ion simultaneously. Fortunately, both MgII and FeII each have two lines visible in the STIS E230H spectral range, so this process can be used for both ions. To conduct a simultaneous fit, the three Gaussian parameter guesses for one line are set equal to the other line's parameters. `GISMFIT` then fits both lines as though they are both limited to sharing the same values with each other for each parameter. While the three Gaussian values may vary subtly for different ions in the same cloud, as discussed in Section 3.1, these parameters should be identical for lines of the same ion, so one MgII or FeII line can serve as a strong check on the validity of its counterpart's fit.

This method also is a useful check upon the accuracy of the reconstructed continuum over an absorption feature. If the continuum for one component is off, the simultanenous fit will not be likely to achieve an absorption profile that reasonably matches the absorption feature for both lines. A simultaneous fit that does well for both lines of one ion is a likely indicator of accurate continua and Gaussian parameters.

While usually at least somewhat helpful, simultaneous fitting is not always the be-all and end-all solution when difficulties and uncertainties arise. So far, only single component, unsaturated systems have been discussed, which are the simplest absorption profiles. Different strategies can be necessary for more complex systems. One of these more complex systems is introduced in Figure 3.6.

3.3 Fitting Difficulties

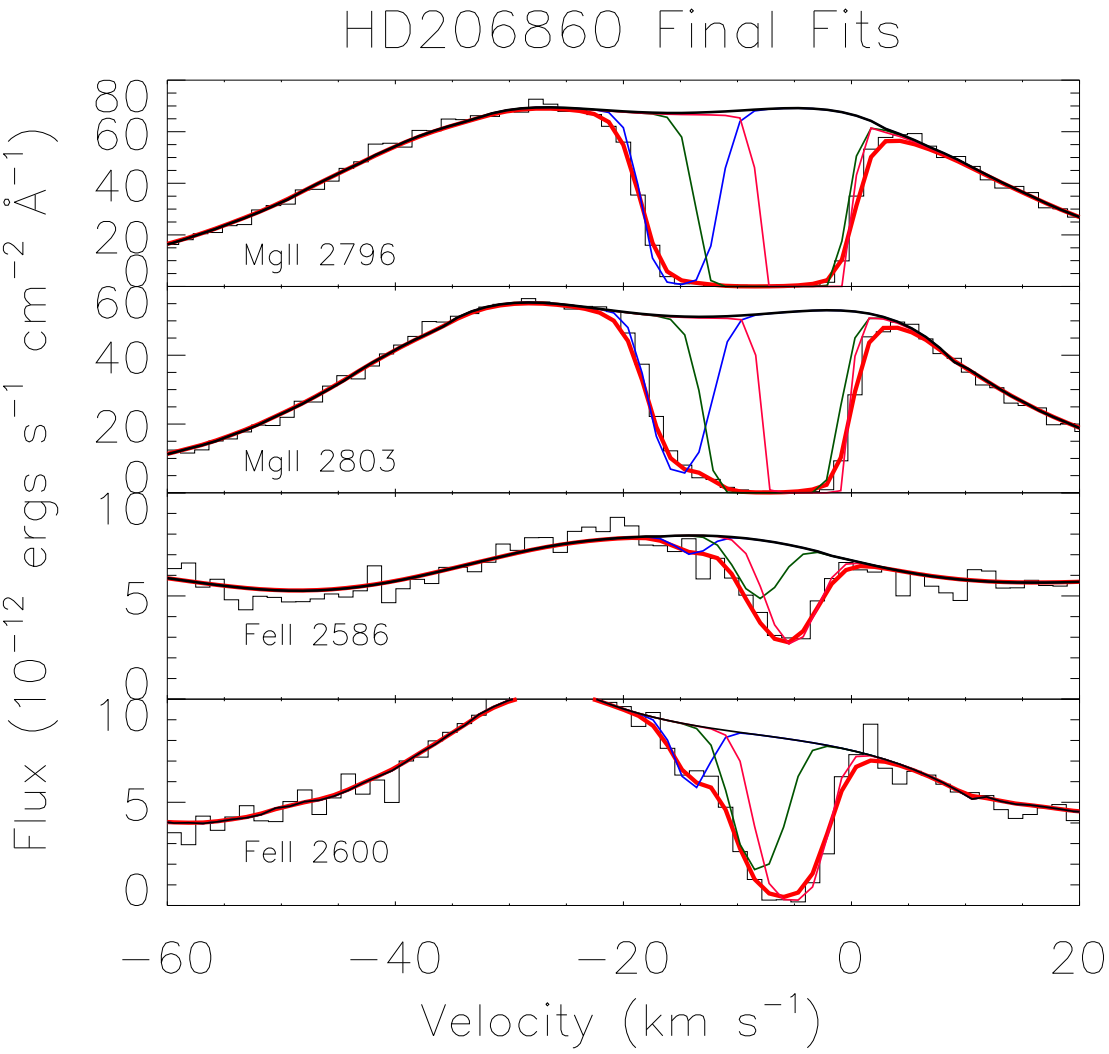

Figure 3.6: These are the final fits for both FeII lines and MgII lines from the line of sight spectroscopic data to HD206860. The three individual components are the thin blue, green, and pink lines that all contribute to the total absorption shown by the thick red line.

The line of sight data for HD72905 provide an extremely simplistic ISM absorption profile. There is only one identifiable cloud and no saturation of any of the MgII or FeII lines. The data is not always so easy to interpret. One prime

example of added complexity is the HD206860 system, shown in Figure 3.6, which provides examples of multiple difficulties that can stymie analysis of an absorption feature.

3.3.1 Multiple Components

Each absorption component is indicative of a single ISM cloud along a line of sight. As indicated by Figure 3.1 in the introduction of this chapter, there are many different known local ISM clouds, with many overlapping in projection. As such, it is not incredibly difficult to procure a line of sight through multiple clouds at once.

If there are numerous components in the data, they will manifest themselves as asymmetries in the observed spectral absorption feature. Ideally, the absorption feature formed by just one absorption component would assume the appearance of a perfect Voigt profile. Multiple components will insert multiple profiles into the absorption feature, creating unique, asymmetrical shapes, such as the absorption features in Figure 3.6.

HD206860's absorption component asymmetry is particularly noticeable in the FeII lines. There is one large asymmetrical Voigt-like profile that must be split into two separate absorption components, and a smaller feature at a higher blueshift that creates a third component. The subtle asymmetries of an absorption feature must be carefully analyzed in order to determine how many absorption components there are along a line of sight.

Also, statistical justification for adding each component comes with the F test. This test compares the reduced χ^2 and the degrees of freedom of the best fit with x number of components to the reduced χ^2 and the degrees of freedom

of the best fit with $x + 1$ components to determine whether improvements in the fit obtained through an extra absorption component can be statistically justified. However, sometimes the F test fails even when there are obvious asymmetries in or other issues with the feature that would justify an extra component. This could happen if the line has an extremely low flux, or if the fit looks reasonable, but the ISM parameters derived from the fit are unnatural. For these reasons, the F test and human judgment are both used to determine the most reasonable number of components.

3.3.2 Blending

The job of determining the number and position of each individual absorption component is often made more difficult by line blending. Line blending occurs when two individual components overlap to some degree in velocity space. HD206860's second and third absorption components provide an example of this phenomenon. In Figure 3.6, it is plain to see the significant blending of the two rightmost absorption features for both of the MgII and FeII lines. The component farthest to the left also blends to a lesser degree with the middle component.

This blending can make it difficult to determine where precisely each absorption component is situated relative to its neighbors. With highly blended lines, `GISMFIT` will often find many plausible solutions to fit the absorption, and it can be difficult to determine which is the most accurate. Careful analysis of absorption feature asymmetries and simultaneous fitting can be helpful on this front, but satisfactory fits still may be difficult to come by, particularly in cases where large amounts of saturation are involved.

3.3.3 Saturation

If an absorption feature is saturated, that means that the flux goes down to or near zero. This means that the maximum amount of absorption for that particular line at that particular wavelength has occurred, and any extra absorption after that point has a diminishing impact on the absorption line shape.

Saturation occurs when there are large column densities for an ion along the line of sight, and this is more likely at longer distances from the Sun. With longer distances, there is the opportunity to accumulate higher column densities. HD206860's MgII lines in Figure 3.6 provide fine examples of saturated absorption features. The two reddest components are both extremely saturated in both MgII lines, as shown by them both flattening out near zero in the vicinity of those absorption components.

Because the Voigt-like shape of the absorption feature is lost at saturation, it can be difficult to determine the number of components and the Gaussian parameters for each feature. However, in this case, FeII can be used to put constraints on the amount and location of absorption components, because the FeII lines are not saturated like the MgII lines. There is only the difficulty of blending of multiple components to deal with.

This is why it is particularly fortuitous to not only have multiple lines of the same ion available in the STIS spectral data, but to also have different ions available to fit as well. Oftentimes, if MgII is saturated along a line of sight, FeII will not be, and can be used to constrain MgII. On the other hand, if the FeII lines show up as extremely weak features, the MgII lines will likely be strong enough to help constrain FeII.

Each line works in concert to constrain the others in order to achieve the most

accurate fit possible, even in particularly complex systems.

3.4 Alternative Ions

While MgII, FeII, DI, and, particularly, HI Lyα are the most important ions in terms of this project, there are other ions that could potentially appear in the spectral range of the data that could be analyzed as well. Each measurement of absorption from another ion adds more weight to final measurements. Redfield & Linsky (2004a) measured a good sample of the available alternative ions such as CII, OI, and SiII, which will be considered here in terms of the HD9826 and HD192310 data sets.

All of these ions can be found within the 1144-1729 Å E140M, medium resolution wavelength range, which means that it is more difficult to distinguish between individual absorption components than for MgII and FeII observed in E230H at high resolution. Because of this, for each alternative ion fitting, the difference in velocity between the established absorption features from MgII and FeII fittings were fixed. The rest of the inputs were allowed to vary.

Unfortunately, there were not many viable absorption features to fit for alternative ions in this data set. For SiII and NI, the signal to noise ratio (SNR) was far too low. The SNR divides the strength of the emission feature by the size of the error in the data. For this data set, the SNR was calculated to be the average SNR value over the emission feature. Any signal of emission for SiII and NI was completely eclipsed by the noise. For example, in the HD9826 data set, the SNR for the SiII 1190 Å and 1194 Å lines both come out to 0.2. This is extremely low. Any number less than one means that the noise is larger than the signal, so no conclusions can be made from the data. Figure 3.7 shows just how noisy the data

is in the vicinity of these two lines. As shown in Table 3.1, the average SNR for the two MgII lines from HD9826 is 28.2. There is almost thirty times as much signal as there is noise, which makes results for this line significant.

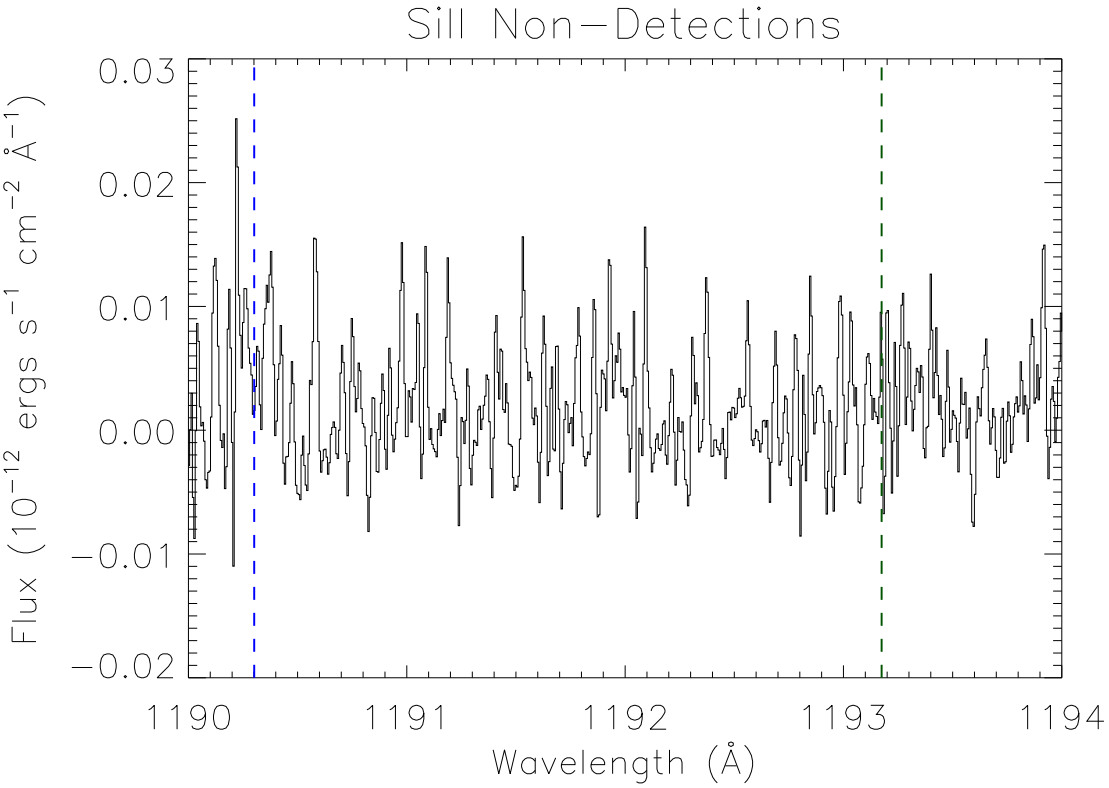

Figure 3.7: The spectral data near the SiII 1190 Å and 1194 Å lines. The place where the 1190 Å emission feature should be is shown with a blue vertical dashed line. For the 1194 Å feature, the dashed line is green. With extremely low SNRs for these two lines, no emission features can be discerned.

Even when the SNR is sufficient to distinguish emission and absorption, other difficulties may arise. For example, because of the low resolution it may be difficult to create a reasonable multiple component fit for a line. However, in the case of OI for HD9826 and CII for HD192310, reasonable fits could be achieved. They both served to successfully corroborate evidence for absorption found in their respective MgII and FeII counterparts, as reasonable fits for three components with the same velocity spacings and ranges as MgII and FeII for each data set were achieved.

Table 3.2: Alternative ISM Fit Parameters.

Object Name	Comp. Number	Ion	Radial Velocity (km s^{-1})	Doppler Width (km s^{-1})	Column Density (log cm^{-2})	SNR
HD9826	1	OI	$9.59 \pm 0.1.18$	4.61 ± 0.59	13.56 ± 0.19	7.5
	2	OI	13.59 ± 1.18	2.42 ± 1.12	13.57 ± 0.60	7.5
	3	OI	17.60 ± 1.18	2.07 ± 14.47	14.47 ± 1.05	7.5
HD192310	1	CII	-29.77 ± 0.87	6.04 ± 1.77	13.46 ± 0.16	2.0
	2	CII	-23.76 ± 0.87	2.38 ± 1.02	15.15 ± 0.44	2.0
	3	CII	-18.77 ± 0.87	5.26 ± 0.72	13.64 ± 0.46	2.0

The more evidence for constraining the ISM values the better when it comes to fitting the most complex line for this project.

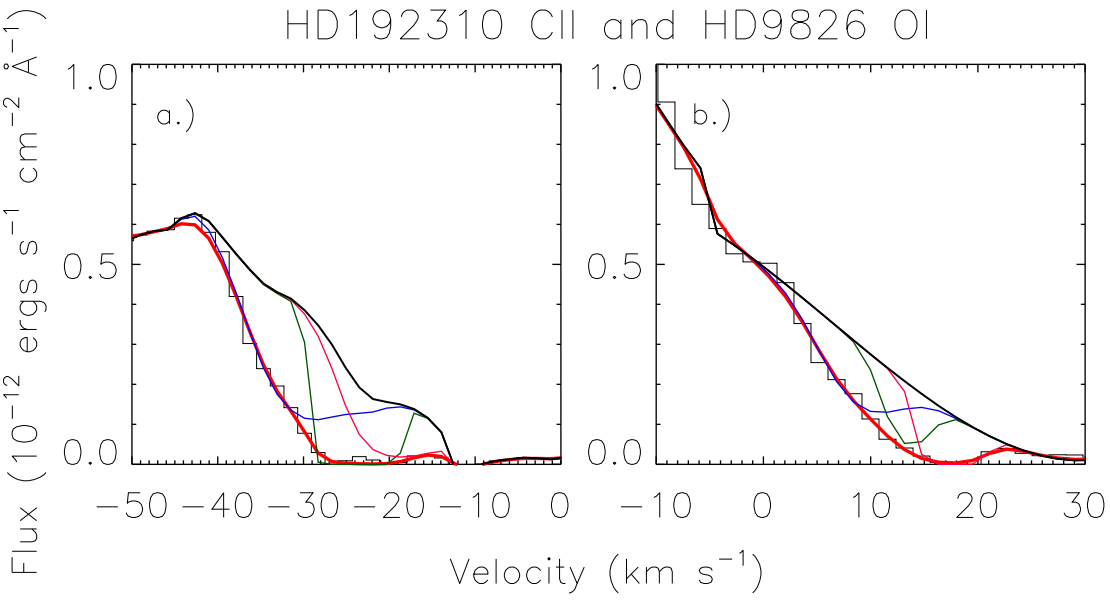

Figure 3.8: The two successful fits for alternative ions in the lower resolution wavelength regime. Each of the three individual absorption features are shown in red, green, and blue respectively. The results for these fits are shown in Table 3.2. Notably, the SNR for these ions is considerably lower than for MgII, FeII, or D1. The flux for the CII emission feature does not even reach 1 * 10^{-12} ergs s^{-1} cm^{-2} Å^{-1}.

Chapter 4

Lyman Alpha

4.1 About the Line

Once the ISM ions discussed in Chapter 3 have been measured to satisfaction, the results become of great use when tackling the next obstacle on the search for stellar wind strengths: Lyα. This line is the first transition in the Lyman series, which is a series that is used to describe the transition of the hydrogen electron from a higher energy state to the ground state, or vice versa. In particular, Lyα describes the lowest energy transition of the electron in this series - from a principle quantum number of 2 to 1.

It occurs at 1215.6700 Å, well within the ultraviolet spectrum accessible with STIS. All subsequent Lyman lines are at too low of wavelengths to be found within the STIS range or any other *HST* instrument (Hernandez 2011). The nearest line is Lyβ at 1025.7222 Å. This makes Lyα the lone Lyman representative to possibly be investigated with this telescope. Luckily enough, this representative is more often than not filled to overabundance with informative absorption to supplement the utter lack of other Lyman members, as is presented by Figure 4.1.

It is a line that, even at close distances such as are being considered for the stars in this project, will be heavily saturated. The DI absorption nearby the Lyα line center, as shown in Figure 4.1b serves as a counterbalance to the saturation

issue by making use of the known D/H ratio of 1.5 $\times 10^{-5}$ (Linsky & Wood 1996), while the geocoronal emission pointed out in Figure 4.1c helps to constrain line center.

It is a difficult line to fit - certainly the most challenging line in this data set to contend with by far. There are many unique pieces working together to extract information from such a complicated line profile, as will be explained through this chapter.

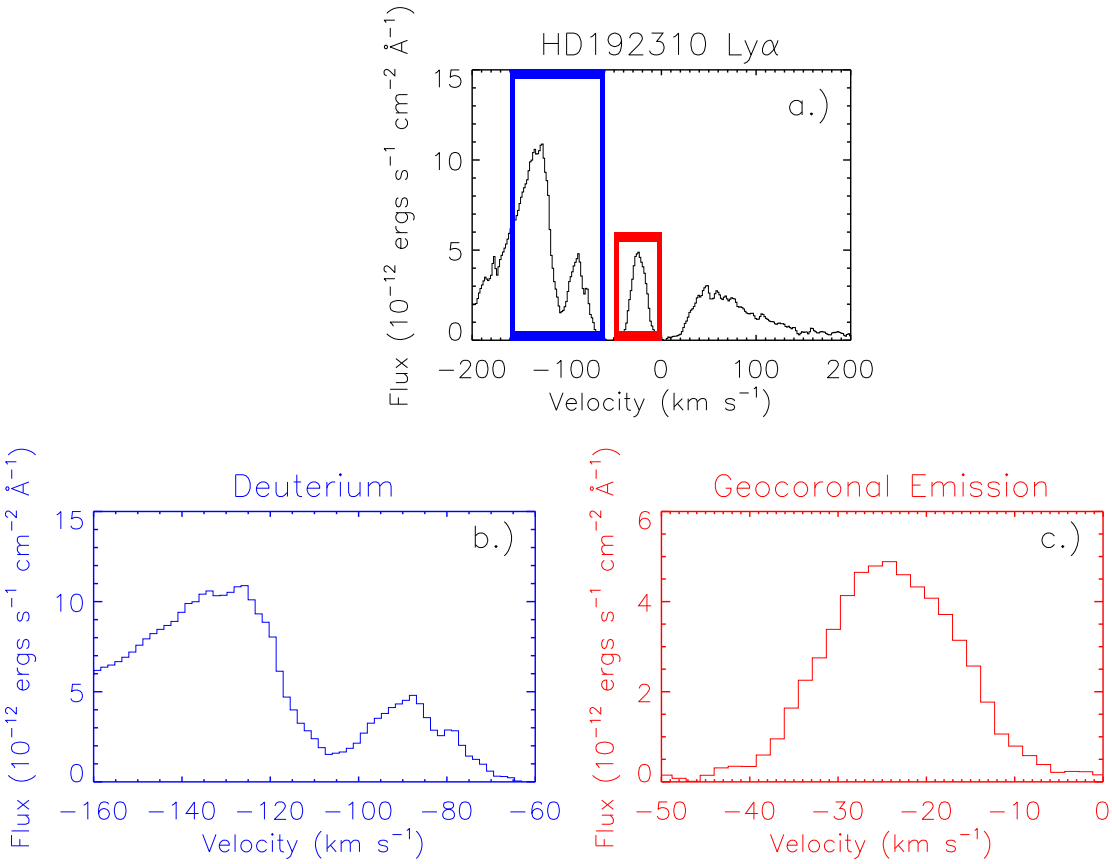

Figure 4.1: Figure a.) is a plot of a typical Lyα feature after abundant absorption occurs along the line of sight. Figure b.) highlights the deuterium feature discussed in Section 4.2.1. Figure c.) shows the geocoronal emission in the Lyα line, which is considered in section 4.3.

4.2 The Over-Saturation Conundrum

Chapter 3 introduced the concept of line saturation in terms of MgII, which, when compared with the saturation of Lyα in this data set, begins to look like a terribly mild case. Figure 4.1a provides a view of how the Lyα line, pre-reconstruction, is absolutely demolished by absorption. So much absorption takes place in the ISM along the line of sight that saturation occurs in spades. For HD192310, this means complete saturation particularly along the region $\pm$50 km s^{-1} shifted from the center of the line. The difficulty with saturation, as discussed in the previous chapter, comes from the loss of information. A majority of the line has been absorbed away, which makes in near impossible to reconstruct a continuum based on clues of the shape left by the remaining emission. `MKFB` is not the solution to reconstructing the continuum this time. This is where the previous ISM ions must come into play.

4.2.1 The D/H Ratio

The unsaturated absorption 81.6 km s^{-1} blueward of the saturated ISM absorption is caused by DI and is intimately tied to the fundamental characteristics of HI Lyα. It is an isotope of hydrogen that is composed of one proton and one neutron, as opposed to the standard hydrogen that consists of one proton and no neutrons. Conveniently, DI has a transition at 1215.339 Å, right next to HI Lyα and shown up close in Figure 4.1b. As isotopes of hydrogen, both HI Lyα and DI have extremely well known abundance ratios in the local interstellar medium. Observations done with the Goddard High Resolution Spectrograph (GHRS) on *HST* have measured the ratio to be $(1.5 \pm 0.10) \times 10^{-5}$ (Linsky 1998).

As shown in Figure 4.1, while HI Lyα is rife with saturation, DI is not saturated at all. Thus, by using known ratios and tying the fit properties of HI Lyα to deuterium, a reasonable fit for the ISM absorption for HI Lyα can be achieved!

4.3 Geocoronal Emission

Before attempting a fit for Lyα, it is necessary to remove all hints of geocoronal emission from the spectrum. The geocorona is a layer of neutral hydrogen atoms at the upper levels of the Earth's atmosphere stretching even beyond the *HST*. Radiation from the Sun can cause these hydrogen atoms to emit, including at the Lyα wavelength, forming a small peak of emission in the Lyα line in the spectral data, as seen in Figure 4.1c. This emission is not part of the stellar emission or ISM absorption along the line of sight, and should not be removed before fitting the line.

Using `GISMFIT` to approximate the feature as a Gaussian, it is then quite a simple task to remove it from the flux of the saturated line. Also, removing this feature serves as an excellent wavelength calibration for the data. The geocoronal emission occurs at line center for Lyα, and any offset of the Gaussian implies a systematic offset of the data itself. The offset values for this data set are shown in Table 4.1.

An average offset of 0.28 km s^{-1} means that instrumental offsets for Lyα and DI will be small, which is something that should be considered if the measured velocity of the Lyα and DI absorption is discrepant with measurements of other ions, such as MgII and FeII. On the other hand, if the DI and HI Lyα absorption aligns closely with the MgII and FeII measurements and the geocoronal offset is small then all evidence points towards a good fit with regards to velocity space.

Table 4.1: Geocoronal Velocity Offset

Object Name (1)	Velocity Offset (km s^{-1}) (2)
HD9826	$+0.91 \pm 0.14$
HD35296	-1.47 ± 0.04
HD72905	$+0.87 \pm 0.03$
HD192310	-0.04 ± 0.00
HD206860	$+1.15 \pm 0.03$
Average Value	+0.28

This table provides the offset values calculated through measurement of the center of the geocoronal emission feature in Lyα, with the wavelength error associated with the Gaussian converted to velocity error through the error propagation technique for a function of one variable given in Taylor (1997) ($\delta v = v\sqrt{(\frac{\delta\Delta\lambda}{\Delta\lambda})^2}$). The average offset of the five lines is quite close to zero.

4.4 The Fitting Process

4.4.1 The Continuum and `LYMANGAUSS`

Because of the large amount of absorption that has taken place, simply using `MKFB` (as is done for MgII and FeII) to reconstruct the continuum using hints from surrounding portions of the spectrum is no longer an effective method. Instead, it is possible to base the continuum off of the stellar emission from MgII. This is a method developed by Wood et al. (2005), with justification gleaned from the Ayres et al. (1995) established correlation between the fluxes of the MgII and HI Lyα lines.

I wrote a program called `LYMANGAUSS` that uses three or four Gaussians to approximate the double peaked shape of the MgII 2796 Å or 2803 Å line emission

feature in the spectrum, and then transposes that continuum over the center of the Lyα line. Since the continua associated with MgII emission lines and the Lyα emission line are from the same star, they will likely be similar in shape, but certainly will not be identical, so this program allows for adjustments to be made to the amplitudes and FWHMs of the Gaussians. Also, the distance between the two peaks can be altered.

The end product is a highly adjustable continuum that can be manipulated quickly and easily as required through the absorption fitting process.

4.4.2 ISM Absorption

As mentioned in Section 4.1, the Lyα fitting process depends heavily on the line's relationship with its nearby deuterium counterpart. Using `GISMFIT`, the two lines are fit simultaneously, with the D/H ratios for column density measured to be $(1.5 \pm 0.10) \times 10^{-5}$ (Linsky 1998), the velocity spacing based on the previously measured MgII and FeII features, and Doppler width determined by the mass difference between the two ions, as discussed in Chapter 2.

Both deuterium and Lyα are doublets, which means that each ISM cloud will show up as two blended absorption components for both lines. In this sample of sight lines, there are spectra with as few as one detected ISM cloud and as many as three clouds. This means that when fitting Lyα it was necessary to fit between four and twelve absorption components simultaneously.

When fitting for Lyα ISM absorption, the velocities, Doppler widths, and column densities are first chosen with the ISM fit values from past fits of MgII, FeII, and DI in mind. With these values, the continuum is adjusted in hopes of finding a reasonable fit. If, after much experimentation, this is deemed impossible,

some of the constraints on the fit values are relaxed, as various potential fits are explored. For example,the velocity spacing between components is initially frozen to MgII and FeII values to see if a reasonable fit can be achieved based on the absorption features measured in higher resolution. If no successful fit is found, the velocity spacing can be freed from MgII and FeII constraints to see if an ideal fit can be unveiled.

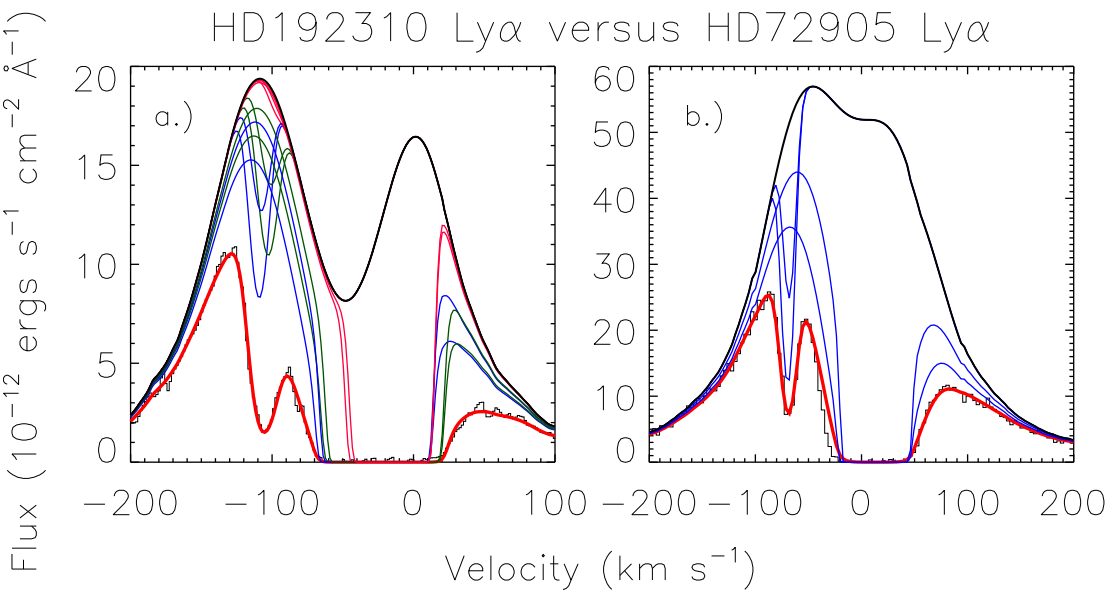

Figure 4.2: These two plots show the end product of a pair of Lyα fits. The red line is the total amount of emission predicted by the fit, while the black histogram line beneath it is the measured flux by STIS. Figure a) shows a successful Lyα fit, where all absorption can be accounted for by the measured ISM features. However, Figure b) shows a Lyα fit that does not match the observed spectrum if only LISM absorption is included. Notice that the red line deviates significantly from the black line in the area of -50 to -20 km s^{-1}. This indicates that there is excess absorption in that region that the ISM components alone cannot account for.

Many factors such as how well each fit matches the present absorption, the similarities or lack thereof of each fit to the previous fits of other ions in the data, and whether or not the measured parameters of a fit could represent a realistic ISM cloud are all taken into consideration when testing the validities of various fits. If a fit can be managed that reasonably satisfies the above criteria then it is

determined that only ISM absorption is necessary to reconstruct the Lyα feature. An example of this is provided by Figure 4.2a. If not, however, absorption from other sources may be necessary to satisfactorily fit the line, which is shown in Figure 4.2b. There is a point in the figure from approximately –50 to –20 km s^{-1}, where the red line does not quite match up the black histogram line. To make this red line dip towards the histogram more blueshifted absorption is needed, which cannot be accounted for by the ISM, because the ISM parameters are tied to and constrained by the DI values. This could indicate the presence of an astrosphere.

4.4.3 Astrospheric and Heliospheric Absorption

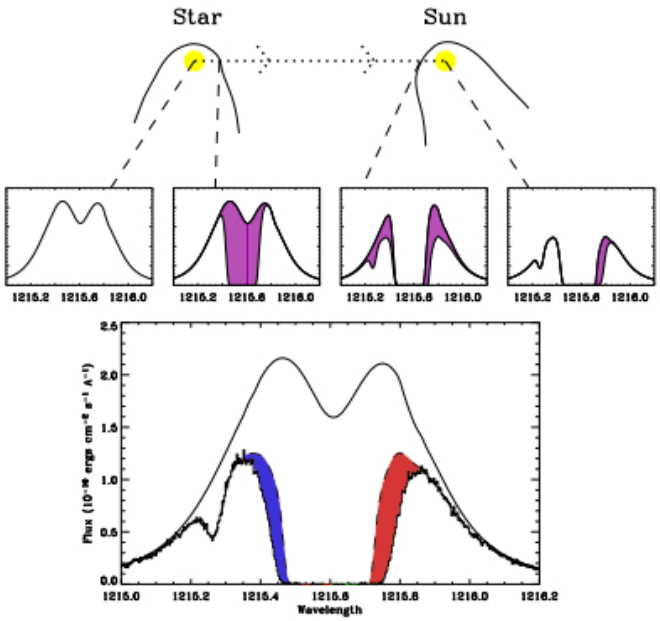

Figure 4.3: This illustration in Wood et al. (2004) demonstrates how Lyα is absorbed along the line of sight. First, extremely blue-shifted light is absorbed via the astrosphere, and can be detected on the left hand side of the Lyα feature, most commonly appearing like the region marked in blue. Next the ISM absorption occurs to saturation levels. Finally, heliosphere causes some extremely redshifted absorption, which shows up in the data like the region marked in red.

Table 4.2: Lyα ISM Fit Parameters.

Object Name	Component Number	Radial Velocity (km s^{-1})	Doppler Width (km s^{-1})	Column Density (log cm^{-2})
HD9826	1	10.83 ± 1.13	13.29 ± 0.30	17.78 ± 0.20
	2	15.11 ± 1.13	7.53 ± 2.19	17.55 ± 0.17
	3	19.02 ± 1.13	9.80 ± 1.74	17.34 ± 0.28
HD35296	1	20.03 ± 0.20	8.08 ± 1.43	17.58 ± 0.08
	2	24.01 ± 0.20	13.56 ± 0.17	17.48 ± 0.10
HD72905	1	12.33 ± 0.19	10.39 ± 0.40	18.13 ± 0.01
HD192310	1	-27.47 ± 0.45	12.69 ± 0.66	17.96 ± 0.03
	2	-21.48 ± 0.45	13.45 ± 0.75	17.90 ± 0.03
	3	-16.47 ± 0.45	11.52 ± 1.42	16.17 ± 0.50
HD206860	1	-16.60 ± 1.16	9.95 ± 1.47	17.35 ± 0.26
	2	-10.76 ± 1.16	12.98 ± 1.08	17.79 ± 0.20
	3	-8.05 ± 1.16	11.97 ± 1.48	18.14 ± 0.17

At the boundary where the stellar winds meet the ISM lies the astrosphere, or, in the case of the Sun, the heliosphere. The physical intricacies of this structure are discussed in more detail within Chapters 1 and 6. What is important in this section, however, is that this boundary is the site of charge exchange between the stellar plasma and the ISM neutrals. A hot, neutral hydrogen wall is formed that is cause for blue-shifted Lyα absorption from astrospheres and red-shifted absorption from the heliosphere, as illustrated in Figure 4.3. The Figure shows the path light takes along the line of sight to *HST*, and how each component of the line is absorbed along the way.

If there is no way to account for some blue-shifted absorption with only the ISM considered for a Lyα fit then a detection of astrospheric absorption becomes likely. The same can be said for red-shifted heliospheric absorption as well. One example of an astrospheric detection is shown in Figure 4.2b.

Table 4.2 shows results for the Lyα fits for the five targets in this data set. An in depth analysis of these results is provided in the following chapter.

Chapter 5

Results

In this section, the measurements of the absorption features gathered from fitting MgII, FeII, DI, and HI Lyα will be analyzed for each sight line. These results will be compared with predictions made with the Redfield & Linsky (2008) dynamical model of the LISM. This model uses information gathered from GHRS and STIS observations of 157 sight lines to make velocity predictions for 15 LISM clouds surrounding the Sun. For given galactic coordinates, the model will calculate which clouds are predicted to intersect the sight line, which clouds are expected to be within 20° of the sight line, and which clouds are expected to be distant from the line (Redfield & Linsky 2008).[1]

To consider comparisons between the model and the measured sight lines for this project, the root-mean-square error (RMSE) will be used:

$$RMSE = \frac{\sqrt{(\sigma_{model})^2 + (\sigma_{observed})^2}}{n} \tag{5.1}$$

In Equation 5.1, σ_{model} is the velocity error associated with the model, while $\sigma_{observed}$ is the velocity error associated with the absorption component in the sight line observed through this project. n is the number of errors considered, which, in this case, will be two. This calculation takes both the observational and modeling errors into account and thus, for absorption component-model comparison, the

[1]The LISM Kinematic Calculator: `http://lism.wesleyan.edu/LISMdynamics.html`

RMSE will be applied to consider the goodness of the match, or lack thereof.

Although many sight lines have been analyzed and contributed towards this model so far, it is far from a perfect picture of 3-D LISM morphology. Each sight line only provides a puzzle piece of the entire picture, limited by the pencil beam line of sight and the distance of the star being observed. Redfield & Linsky (2008) found a third of the clouds they observed to have some filamentary structure, which indicates that many clouds have complex shapes. These are shapes that approximations made to fill in the holes of a limited data set may have difficulty compensating for. Also, around 20% of the measured sight lines in the Redfield & Linsky (2008) analysis could not be attributed to one of the 15 clouds, which implies a need for more data to fill in some gaps.

Considering the complexity of the system and the dearth of available data, uncertainties in the Redfield & Linsky (2008) model should be expected and accounted for. That is why, when considering possible cloud matches for measured absorption features in this data set, both clouds expected to traverse as well as fall within 20° of the sight line will be considered for potential matches.

As a basis for comparison to the Redfield & Linsky (2008) model, mostly MgII absorption feature measurements will be used. Compared with FeII, they have a much higher signal to noise ratio, as shown in Table 3.1, and are much simpler to model than DI and HI Lyα, making them the most consistently reliable lines in the data set. However, for any data set where MgII is entirely saturated at both 2796 Å and 2803 Å, FeII will be used, as there is significant information loss in a saturated feature that makes the lower signal to noise FeII a more palatable case in that scenario.

Comparing the Redfield & Linsky (2008) model to this project's results will be incredibly telling. If a sight line matches the model extremely well, such as is the

case with HD72905, the comparison serves as a good check on the methodology used to obtain results for this project. In the case that this project has a sight line where the model does not predict a reasonable cloud, a little investigation is in order to question the potentially validity of the fit and the strength of the model in that circumstance. In either case, this data set will provide five new sight lines to test and expand the Redfield & Linsky (2008) model.

5.1 HD9826

In the case of HD9826, the two clouds estimated to be found within 20° of the sight line by the Redfield & Linsky (2008) model have a predicted velocity within the errors of one of this project's measured MgII absorption components, as shown in Table 5.1 and Figure 5.2. The component at 12.04 km s^{-1} falls well within the 1σ RMSE errors for the Hyades cloud, while the 16.30 km s^{-1} component lies within the 3σ RMSE errors for the LIC. However, there are only two predicted components for the model - LIC and Hyades - and this project measured three individual absorption components.

The component that does not have cloud-velocity match near to the sight line as predicted by the Redfield & Linsky (2008) model is also the one with the lowest column density for each ion. This means the component has the lowest signal to noise detection of the three. However, the column density is not negligible, and the three component fit for this line successfully passes the F test over the two component fit.

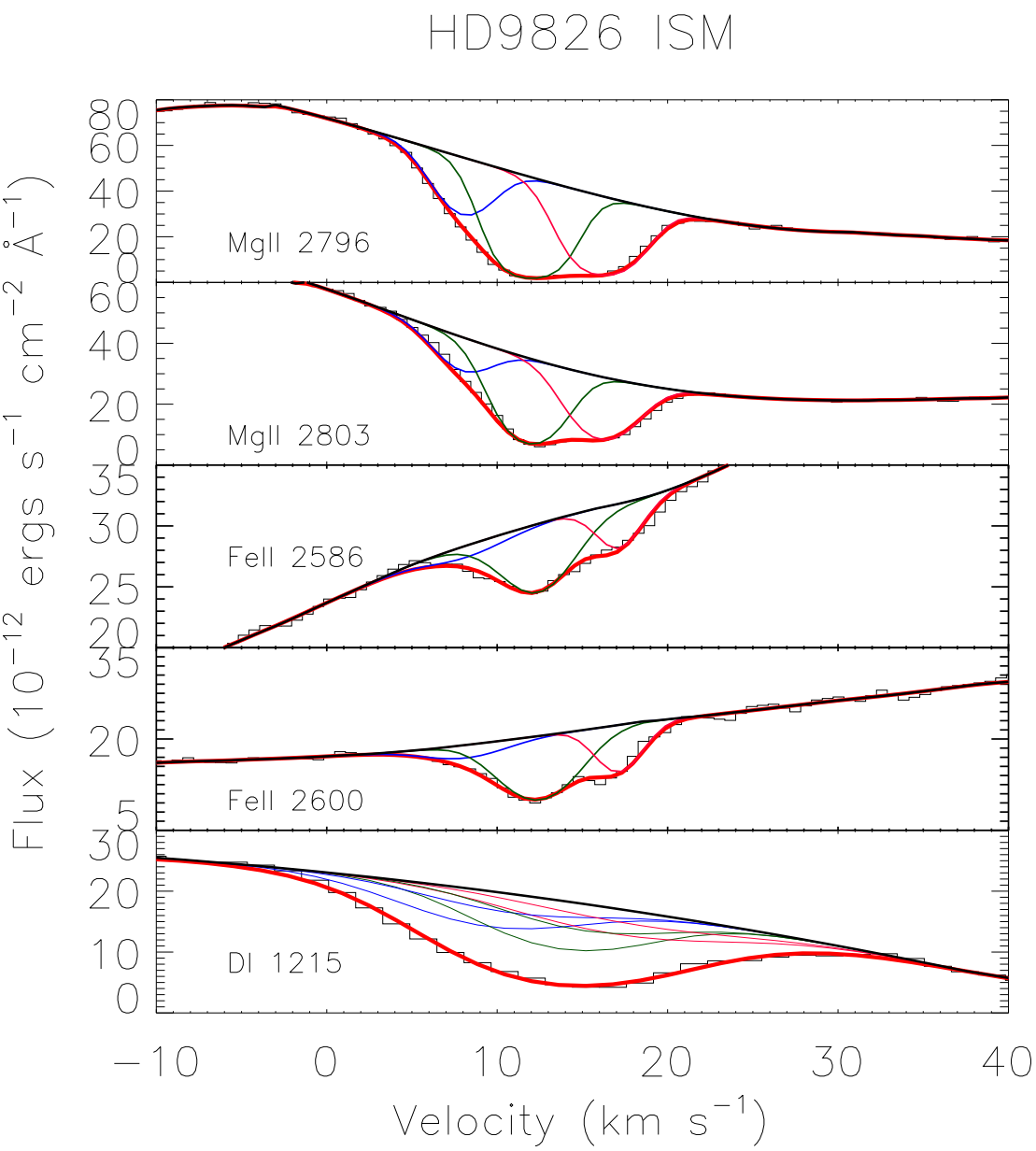

Figure 5.1: The final reconstructed continua and absorption profiles for MgII, FeII, and DI for HD9826. The blue, green, and pink lines represent individual absorption components, while the red line represents cumulative absorption from all components convolved with the LSF. DI has double the expected components (two for each color) because it is a doublet, which means the feature actually contains two lines extremely close to one another at 1215.3376 Å and 1215.3430 Å.

If one looks only at the velocities of the clouds in the Redfield & Linsky (2008) model, and not on their predicted nearness to the sight line, there are a couple

Predicted Cloud Name	Predicted Closeness Degrees	Predicted Velocity (km s^{-1})	Potential Matching Component	Observed Velocity (km s^{-1})
LIC	0.0	14.44 ±1.23	Yes	16.30±0.21
Hyades	3.0	12.06 ±1.19	Yes	12.06±0.16

Table 5.1: The predicted ISM clouds along the line of sight to HD9826 from the Redfield & Linsky (2008) model and their potential matches from the sight line analyzed in this project's data set. A 0° closeness estimation means an intersection of the cloud with the sight line is predicted by the model.

clouds with velocities close to the one absorption component lacking in a cloud match. As demonstrated by Figure 5.2, for a measured velocity of 8.05 ±0.72 km s^{-1}, the two most reasonable predicted clouds are:

i) Mic at 9.53 ±1.57 km s^{-1}

ii) Aur at 6.44 ±1.06 km s^{-1}

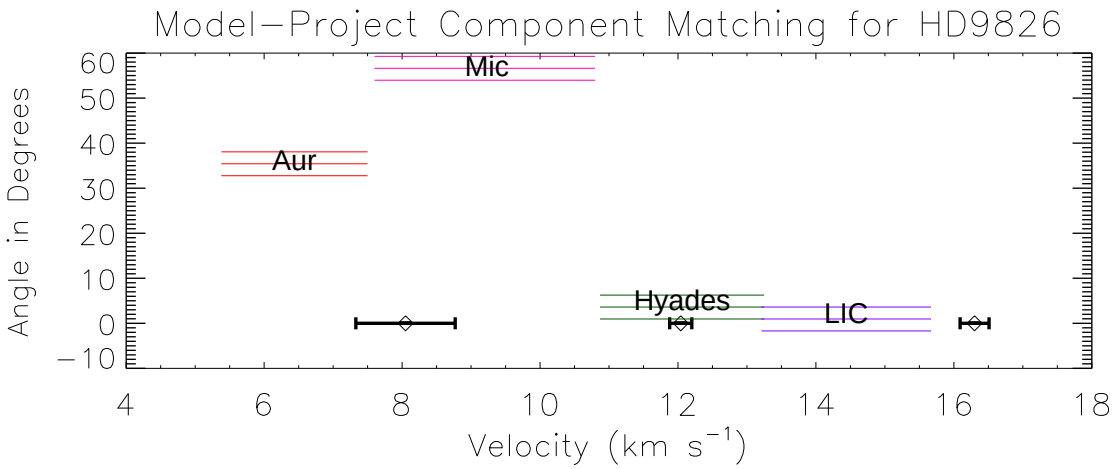

Figure 5.2: The three absorption components for this sight line are plotted with 1σ error bars. The cloud velocities along this sight line predicted by the Redfield & Linsky (2008) model are shown as alternating lined and labeled rectangles, shaded out to the 1σ velocity errors provided by the model. The predicted angle of the clouds away from the line of sight is shown on the y-axis.

However, this absorption component is also the component with the most inconsistent measured velocity between FeII and MgII, with a difference of 2.89

km s^{-1}. For this reason, predictions based only on cloud velocity should be taken lightly in this instance. This final component has the potential to be associated with either of the two clouds listed above.

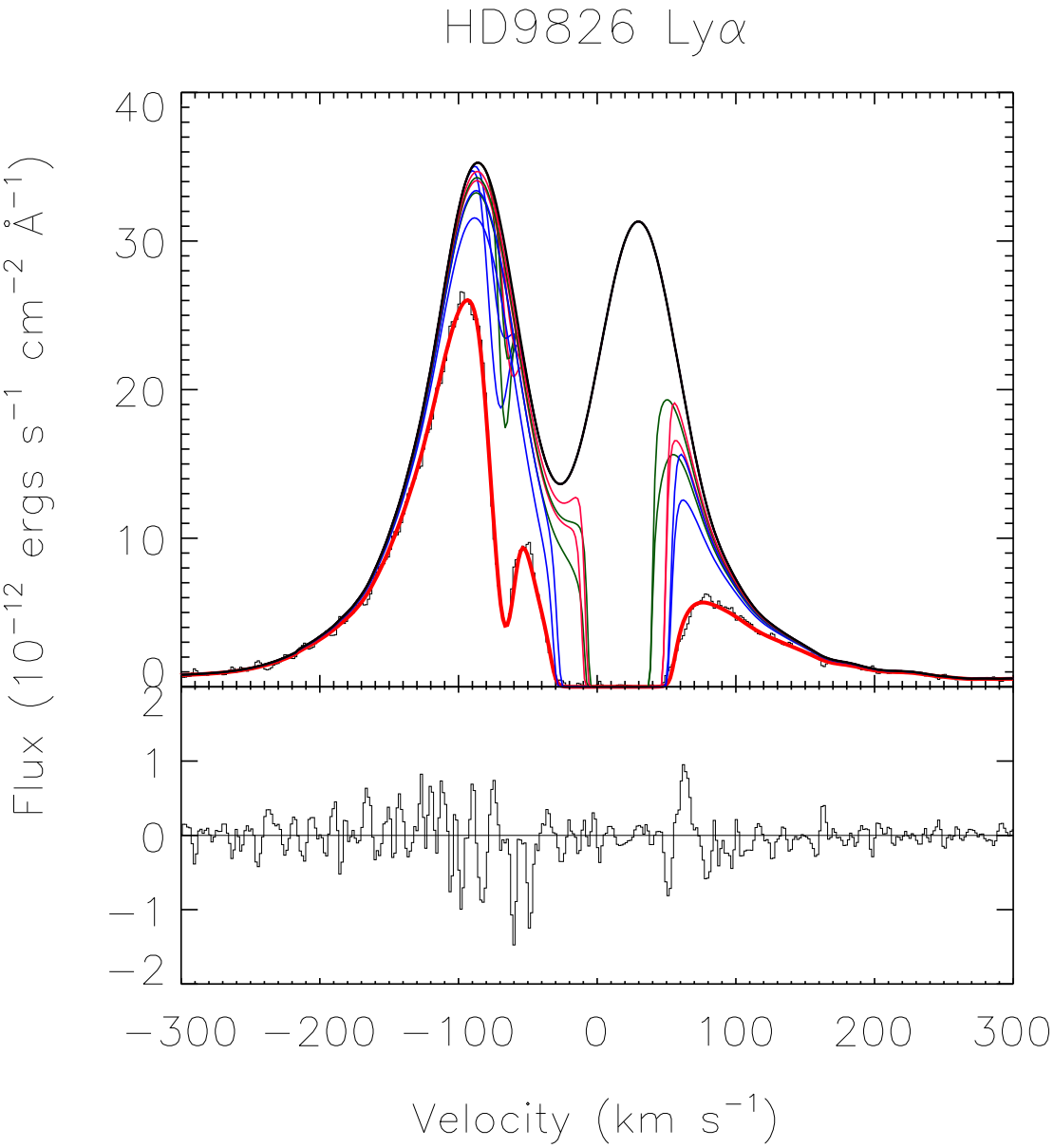

Figure 5.3: The HI Lyα line is simultaneously fit with DI, shown at a blueshift of -81.6 km s^{-1} from HI Lyα line center. Along with DI, HI is also a doublet, so, with three absorption features, DI has six components and HI has six components, making a total of twelve components for this fit. The difference in flux versus the total predicted absorption is plotted in velocity space beneath the fit.

The most likely cloud match when considering the velocities is Aur. It is the closest in predicted angle, is considered filamentary by Redfield & Linsky (2008), and has the smallest associated errors, as demonstrated in Figure 5.2. It is also just as likely that this final component is not associated with any identified clouds, for, as mentioned earlier, 1/5 of the components from the Redfield & Linsky (2008) study were unable to be associated with a specific cloud.

5.1.1 Astrosphere/Heliosphere Detections

For this sight line, there was no astrospheric or heliospheric absorption signal present in the Lyα line. Figure 5.3 shows an excellent match between the measured flux from ISM absorption and the received flux viewed through STIS. A reasonable fit could be achieved with only ISM absorption considered. However, this non-detection does not definitively exclude the presence of an astrosphere around the HD9826 system, and the possibility of a hypothetical detection for this system will be considered in Chapter 6.

5.2 HD35296

For this sight line, there were two measured absorption components, both of which have a velocity within errors of predicted clouds from the Redfield & Linsky (2008) model directly traversing or within 20° of the sight line, as shown in Table 5.2. The component with the largest column density and a velocity of 23.61 km s^{-1} is an extremely good match for the cloud predicted to traverse the sight line: LIC. However, it is also a potential good match for Aur cloud, predicted to be within 20° of the sight line. This being the largest absorption component, it is possible that what this project has identified as one absorption feature is actually

two blended features with extremely close velocities.

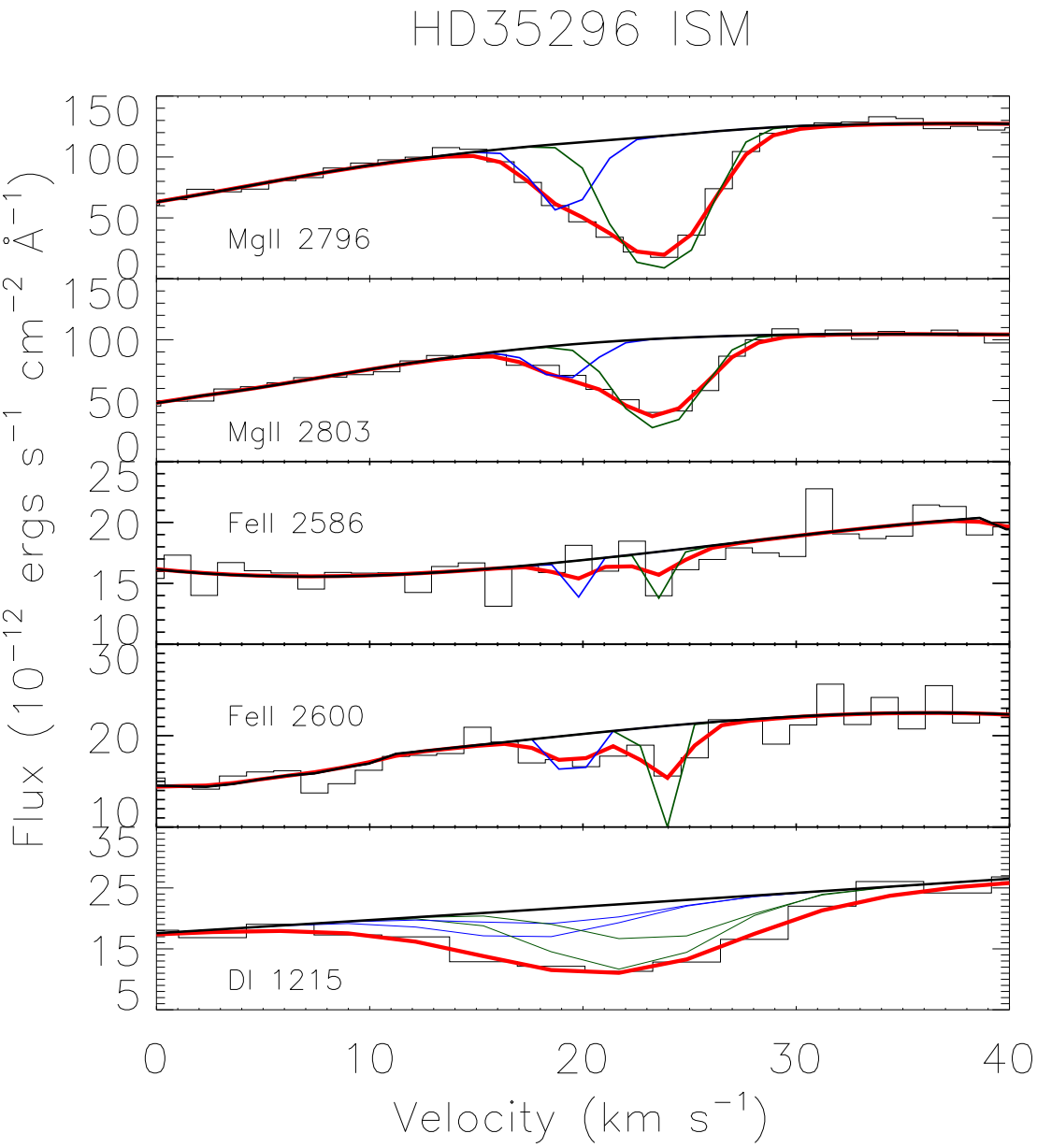

Figure 5.4: Same as Figure 5.1 for HD35296, except there are two individual absorption components (blue and green) instead of three.

This leaves a weaker component with no associated cloud at 19.39 km s^{-1}. As illustrated by Figure 5.5, this component is reasonably distant in velocity space from any of the predicted clouds. It is just outside the 5σ RMSE errors of both

Predicted Cloud Name	Predicted Closeness Degrees	Predicted Velocity (km s^{-1})	Potential Matching Component	Observed Velocity (km s^{-1})
LIC	0.0	23.85 ±0.91	Yes	23.61±0.12
Aur	6.0	22.88 ±0.86	Yes	23.61±0.12
Hyades	9.5	11.54 ±1.20	No	...

Table 5.2: Same as Table 5.1 for HD35296.

the LIC and Aur. However, as the weakest component, it has the largest errors associated with its velocity, and could very well be closer to the clouds' velocities than has been measured to be. On the other hand, there is also the possibility that this absorption feature should not be associated with any predicted clouds just like the 8.05 km s^{-1} component in the HD9826 data set.

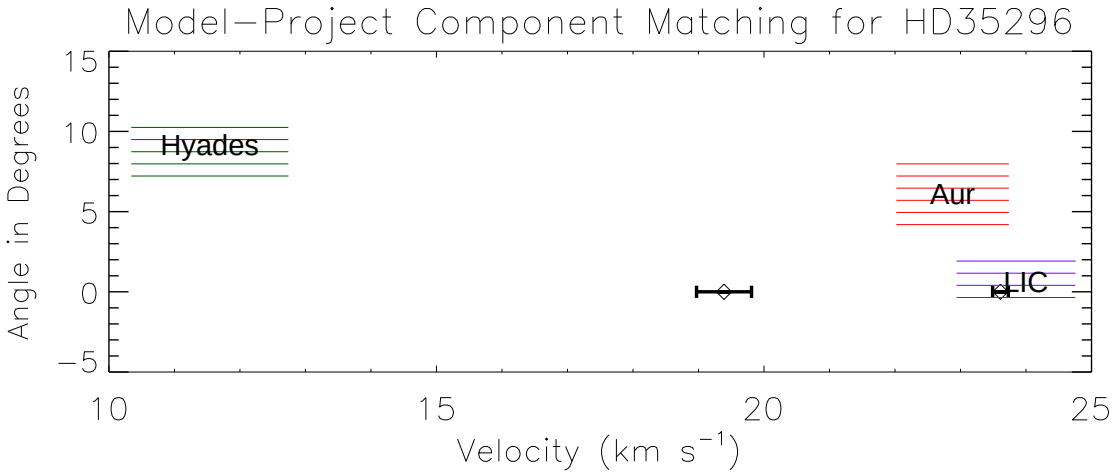

Figure 5.5: Same as Figure 5.2 for HD35296.

One cloud predicted to be with 20° of the sight line - Hyades - has no matching measured component from this project. As the cloud is not predicted to directly traverse the sight line however, this is a reasonable result, and does not diverge from the Redfield & Linsky (2008) model.

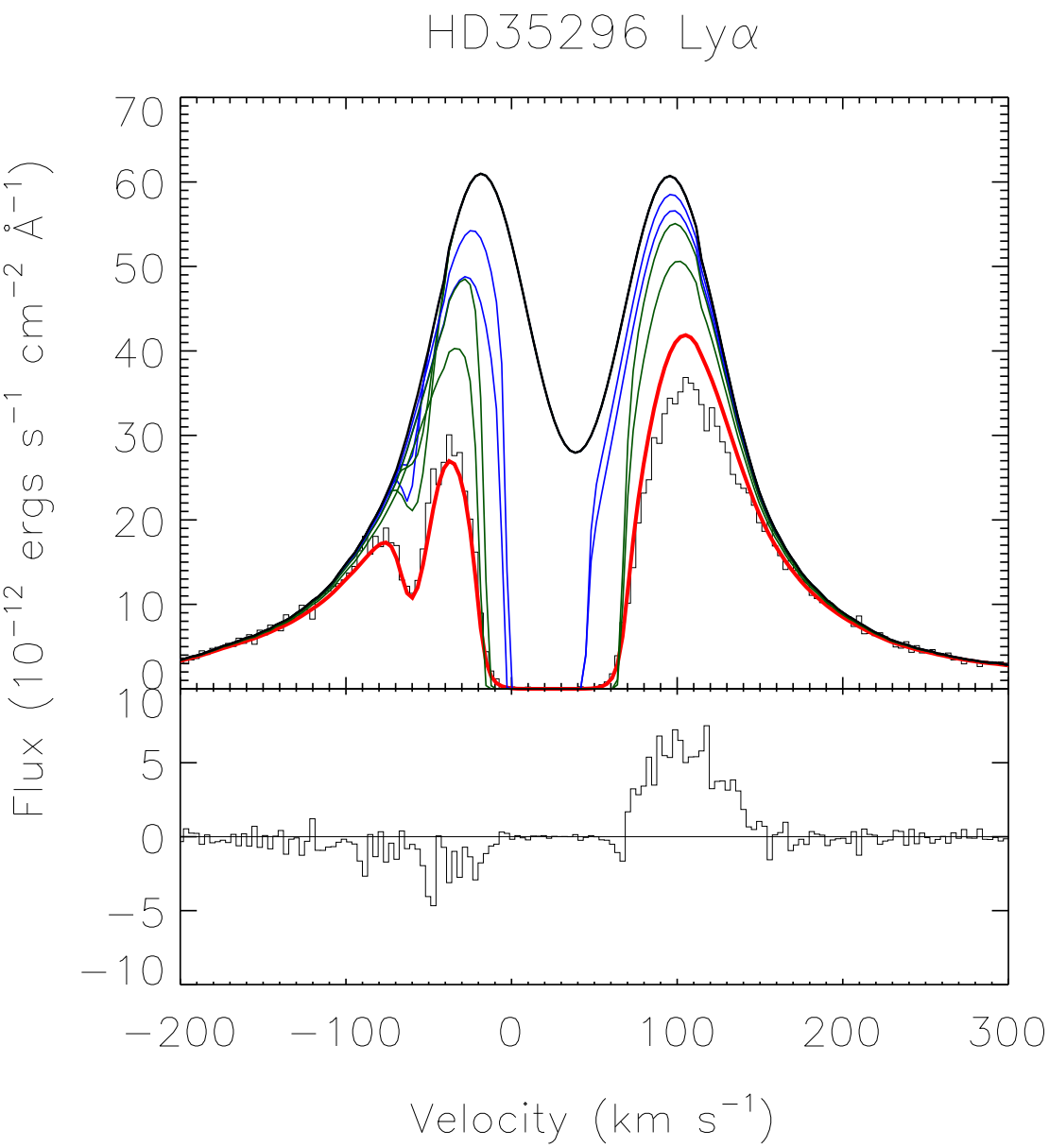

Figure 5.6: Same as Figure 5.1 for HD35296, except there are two individual absorption components (blue and green) instead of three.

5.2.1 Astrosphere/Heliosphere Detections

With all ISM absorption accounted for, there was still excess absorption on the right hand side of the Lyα feature to be dealt with. This feature can be considered a detection of heliospheric absorption.

The detection from this project confirms the detection from Wood et al. (2014a). Wood et al. (2014a) strongly emphasize the importance of this measurement occurring with a sight line downwind of the ISM flow vector. In this direction, the heliospheric absorption can be considered part of the heliotail, which, true to its name, is the tail end of the heliosphere. The shape of the heliosphere is somewhat cometary, as there is a large nose, and long, thin trailing tail, which is the portion measured by this sight line. Constraints on the heliotail are helpful with determining the accuracy of models of heliospheric structure and asymmetries. Heliospheric absorption detections are also important in terms of helping to constrain astrospheric models. The better the structure of the heliosphere around the Sun is understood, the more useful that knowledge will be in terms of applying it to astrospheric structures foreign to the solar system. This process will be considered in more detail in Chapter 6.

5.3 HD72905

This sight line was by far the most straightforward line in the data set. As shown in Figure 5.7, there is only one component at 12.82 km s^{-1}, and that component matches quite well with the single predicted transversing cloud along the sight line, as presented in Table 5.3 and Figure 5.8.

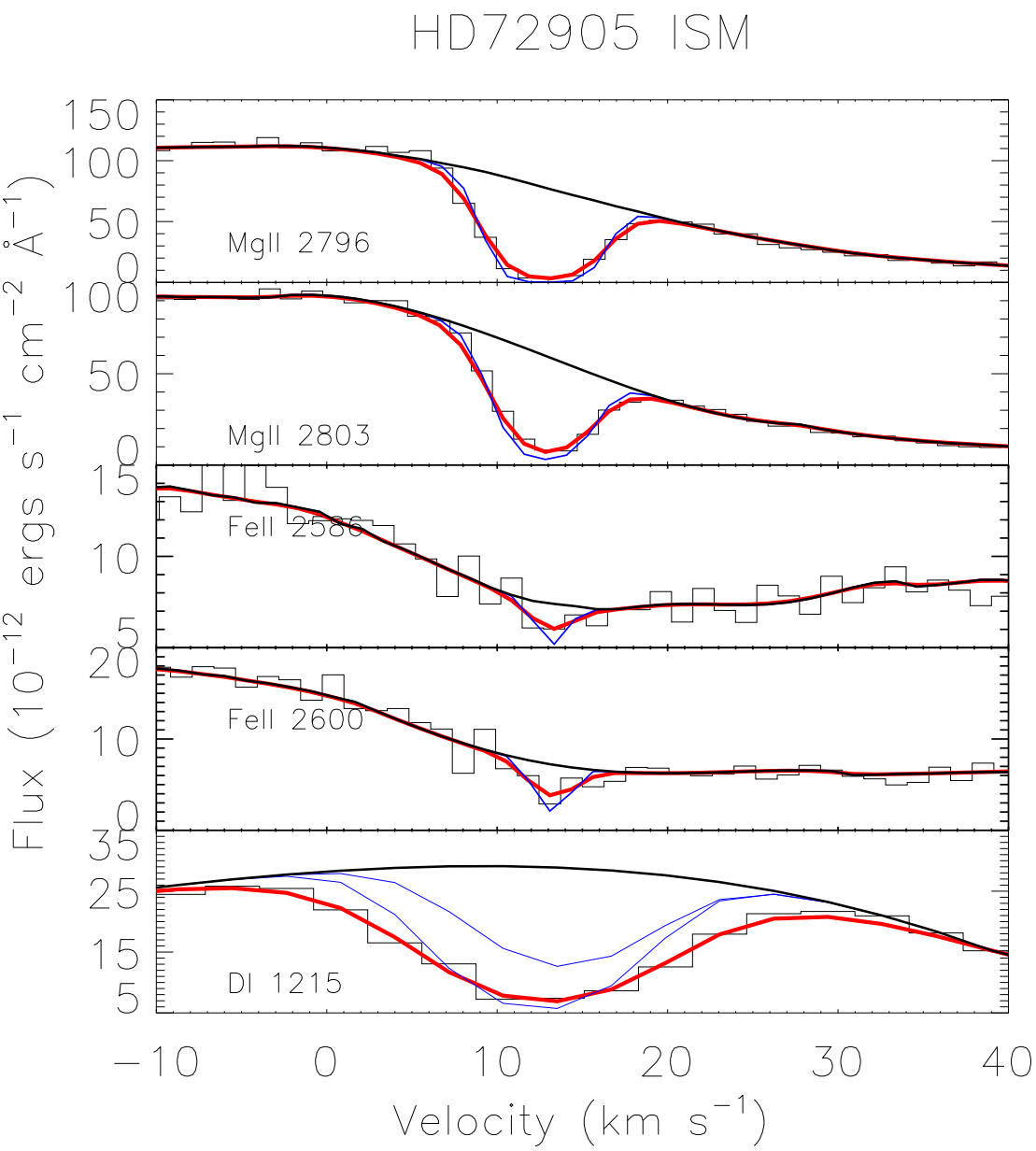

Figure 5.7: Same as Figure 5.1 for HD35296, except there is one individual absorption component (blue) instead of three.

Predicted Cloud Name	Predicted Closeness Degrees	Predicted Velocity (km s^{-1})	Potential Matching Component	Observed Velocity (km s^{-1})
LIC	0.0	11.99 ±1.28	Yes	12.83±0.16
Aur	17.4	5.23 ±1.29	No	...
Hyades	18.7	2.68 ±1.55	No	...

Table 5.3: Same as Table 5.1 for HD72905.

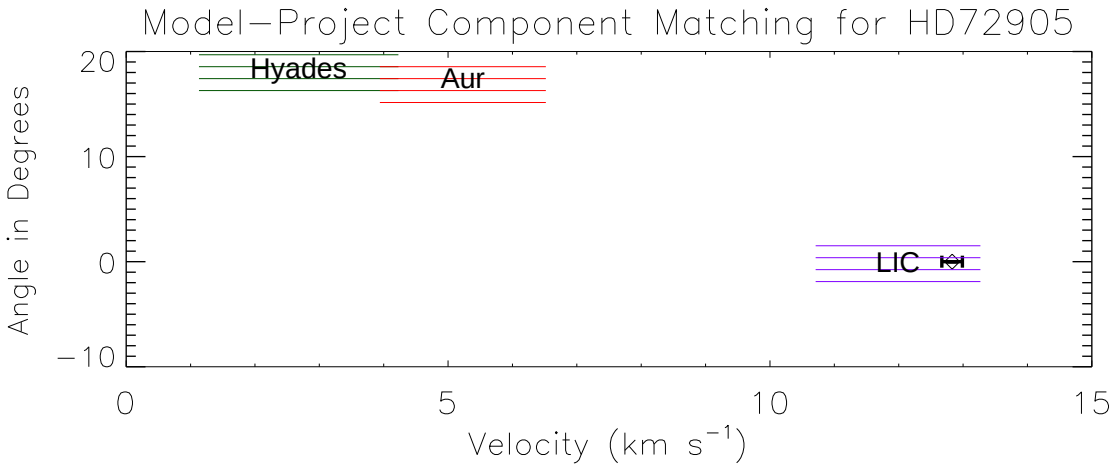

Figure 5.8: Same as Figure 5.1 for HD72905.

5.3.1 Astrosphere/Heliosphere Detections

As shown in Figure 5.9, there is a significant gap between the actual received flux and the flux predicted with absorption only from ISM components on the left side of the Lyα feature. This excess blue absorption is most likely astrospheric absorption from the HD72905 system.

This detection of an astrosphere in the data serves as an independent confirmation of the work of Wood et al. (2014b). Wood et al. (2014b) used their astrospheric detection to model the wind for this young, solar-like star, finding it to be around half as strong as the winds of the present day Sun (Wood et al. 2014b). A discussion of this model will be presented in Chapter 6.

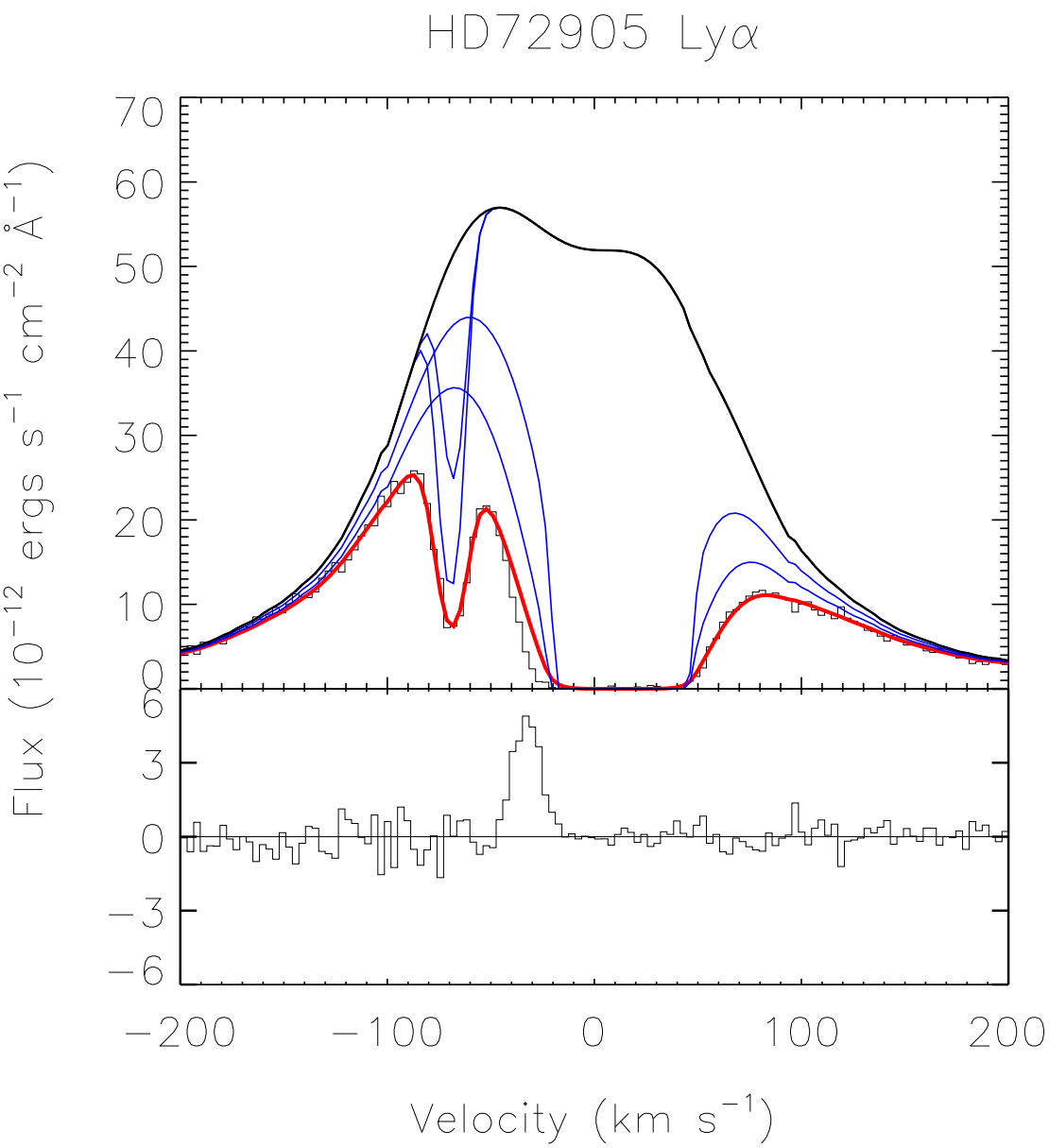

Figure 5.9: Same as Figure 5.1 for HD35296, except there is one individual absorption component (blue) instead of three.

5.4 HD192310

The HD192310 data contains three absorption features per ion, as shown in Figure 5.10. For this data set, because of the heavy saturation of the MgII lines,

Predicted Cloud Name	Predicted Closeness Degrees	Predicted Velocity (km s^{-1})	Potential Matching Component	Observed Velocity (km s^{-1})
Mic	0	–23.74 ±1.02	Yes	–24.04 ±0.51
Aql	0	–9.61 ±1.03	No	...
Vel	9.5	–31.70 ±1.52	Yes	–30.69 ±0.66
LIC	14.1	–17.32 ±1.15	Yes	–19.02 ±2.10
Eri	16.4	–16.40 ±1.14	Yes	–19.02 ±2.10

Table 5.4: Same as Table 5.1 for HD192310.

the FeII velocities are used as the basis of comparison to the Redfield & Linsky (2008) model. The measured velocities for these components match up quite well with four of the five clouds predicted to intersect or be within 20° of the sight line, as outlined in Table 5.4 and Figure 5.11. Two of the clouds within 20° of the sight line - LIC and Eri - have extremely similar velocities and the absorption component in this data set measured at a velocity of –19.02 km s^{-1} could very well belong to either of them.

Actually, the absorption feature could very well be representative of both of them. That single component could in reality be two individual components. However, there is not enough evidence in the data set to satisfactorily claim this assertion. The F test did not support a four component fit.

A quick glance at the MgII lines in Figure 5.10 will reveal how heavily saturated and blended the lines are. A similar look at the FeII lines and Table 3.1 can show how incredibly low the SNR is at a measly 1.3. With so much saturation, it becomes difficult to discern how many individual absorption profiles make up the whole. Looking at the green and red absorption features for MgII, it is reasonable to consider that there might be a third hiding in the midst of the saturation.

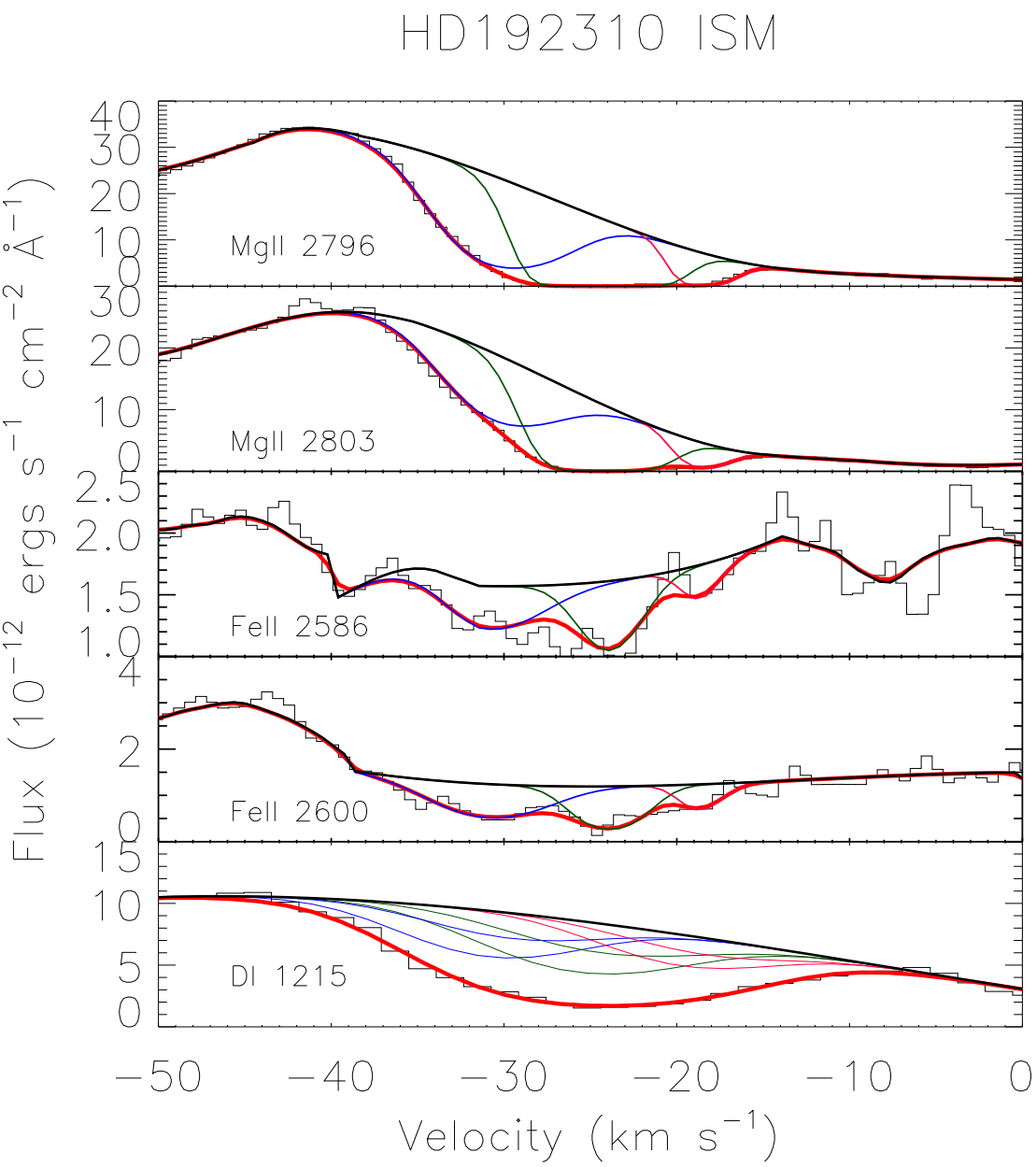

Figure 5.10: Same as Figure 5.1 for HD192310.

The weak FeII lines come with the same problem, but from the opposite angle. The signal is so shallow that how many absorbers, and how much they are absorbing becomes a difficult question to answer. In the end, through a combination of F tests and simultaneous fits, comparing MgII and FeII against each other, only

three components could be reasonably justified within this project's methodology.

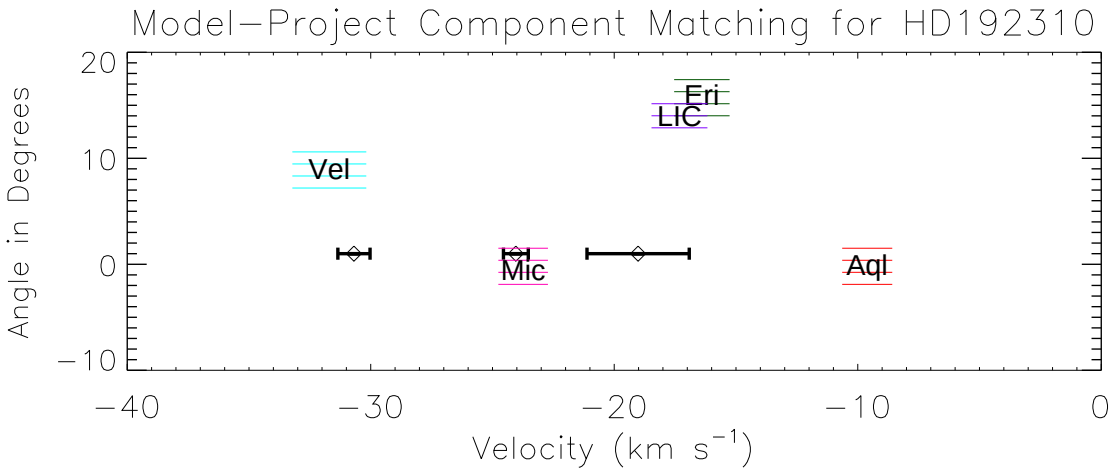

Figure 5.11: Same as Figure 5.1 for HD192310.

The one cloud that did not appear to correspond well with any measured components - Aql, shown in red in Figure 5.11 - is a cloud that the Redfield and Linsky model predicted would directly intersect the sight line. It is not within 5σ of the RMSE of the closest absorption feature, and this is the feature much more closely aligned with the two clouds discussed in the previous paragraph. However, because of the saturation issues, it is possible that yet another unique component lies hidden in that absorption feature that could align with more closely with Aql's predicted velocity.

Just as discussed earlier, there is the possibility the green and red absorption features could be hiding a third component in their midst. It is possible that this component could lie closer to line center than any of the others, putting it in closer alignment with Aql. However, the saturation of the MgII lines and the low signal of the FeII lines makes this scenario impossible to statistically justify for this sight line.

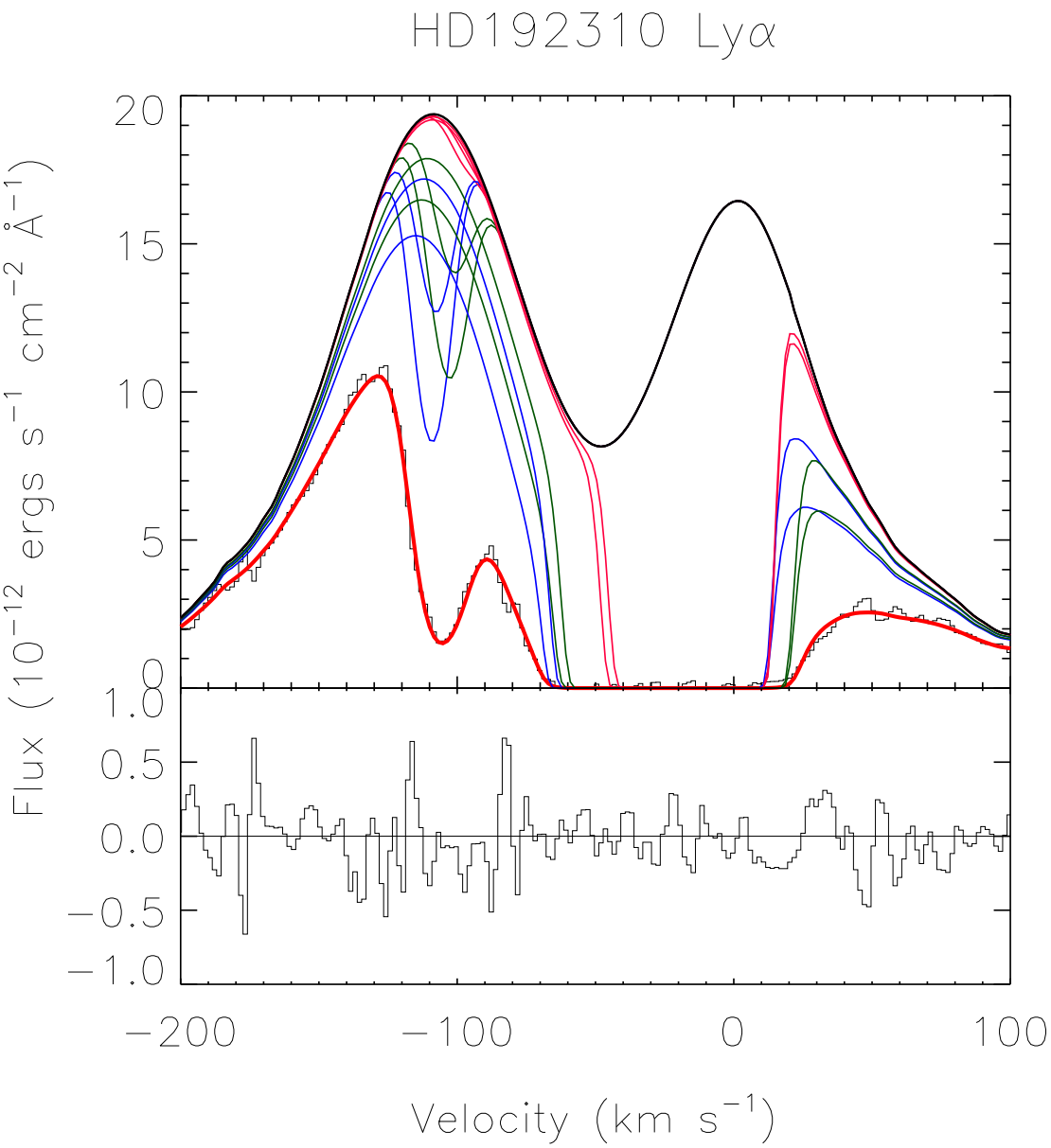

Figure 5.12: Same as Figure 5.1 for HD192310.

5.4.1 Astrosphere/Heliosphere Detections

Like HD9826, HD192310's Lyα feature was able to be reconstructed reasonably with only ISM absorption, as shown in Figure 5.12. Also like HD9826, a hypothetical astrosphere for this sight line will be considered in the following

chapter.

5.5 HD206860

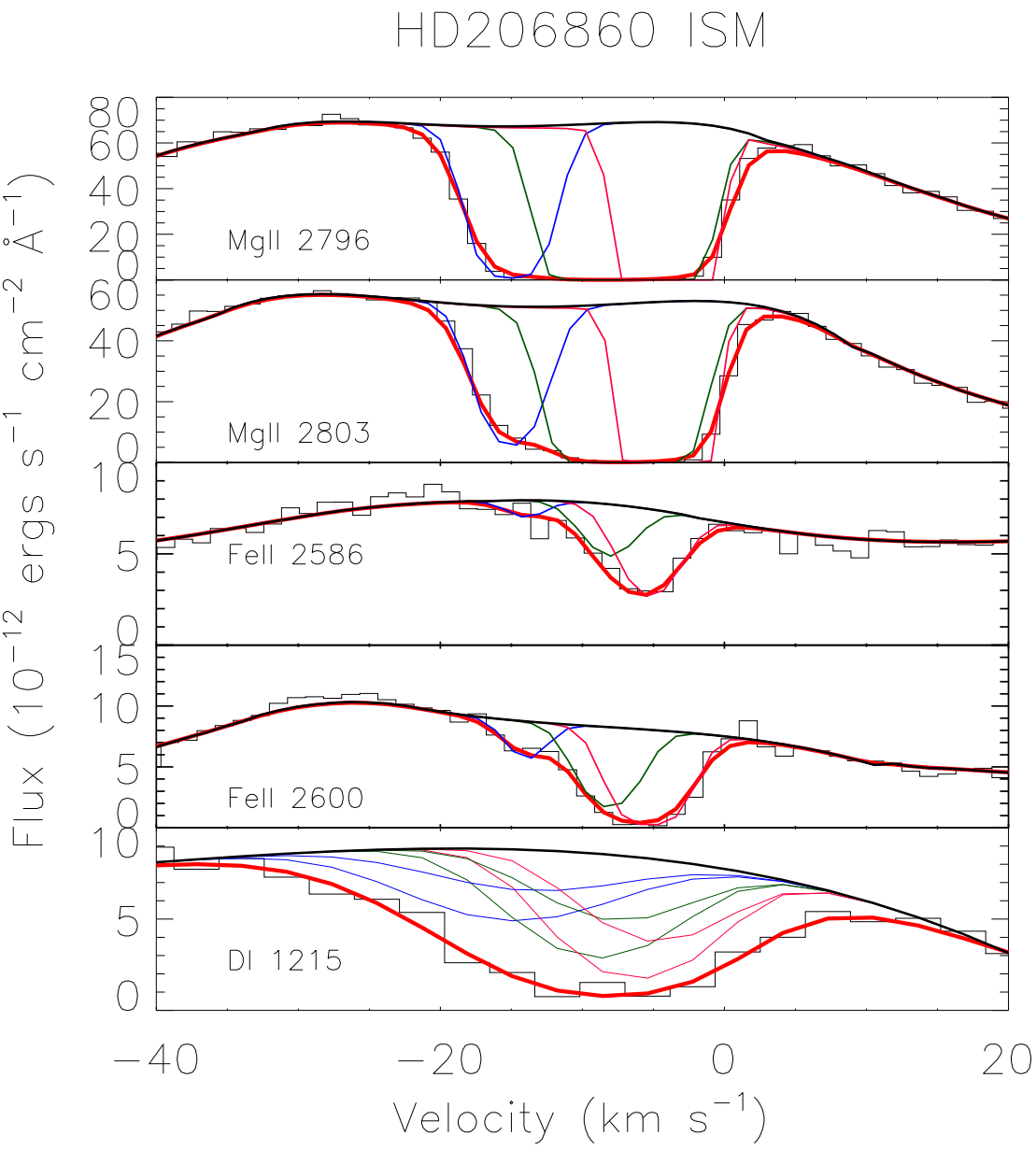

Figure 5.13: Same as Figure 5.1 for HD206860.

Predicted Cloud Name	Predicted Closeness Degrees	Predicted Velocity (km s^{-1})	Potential Matching Component	Observed Velocity (km s^{-1})
Eri	0.0	–8.65 ±0.99	Yes	–7.14 ±0.91
Aql	10.0	6.63 ±0.99	No	...
LIC	11.0	–6.70 ±1.35	Yes	–5.00 ±0.65
Hyades	19.2	4.01 ±1.68	No	...

Table 5.5: Same as Table 5.1 for HD206860.

The final sight line in the set has three measured absorption components, as shown in Figure 5.13. The saturation is quite severe with MgII, but the velocities of the measured components line up well with two of the four predicted clouds, as outlined in Table 5.5 and Figure 5.14. There is not a component whose velocity is reasonably close to Hyades and Aql, but these two clouds are only predicted to be close and not to directly intersect the line, so this result does not fall out of line with Redfield and Linsky's model.

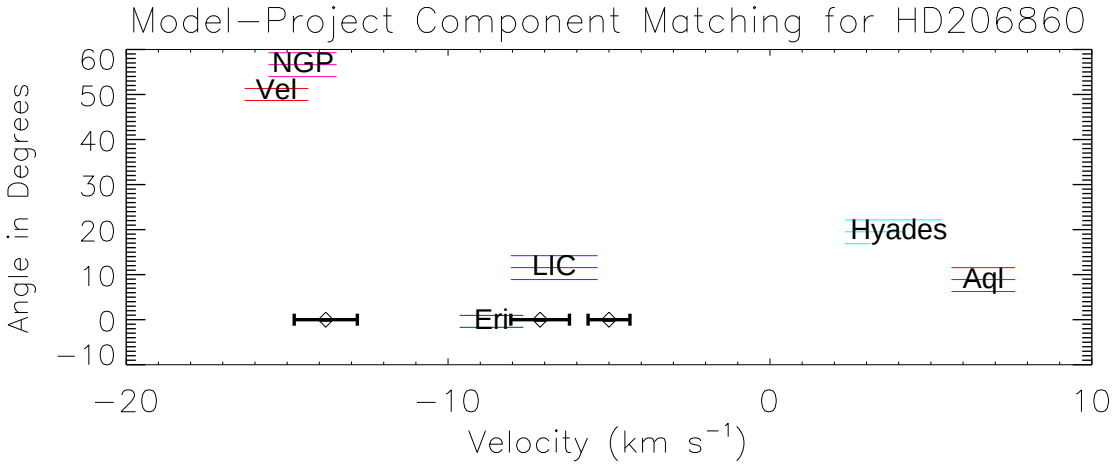

Figure 5.14: Same as Figure 5.1 for HD206860.

The one major anomaly is that there is an absorption feature whose velocity does not match that of any of the nearby predicted clouds. At –14.77 km s^{-1}, this feature most closely matches the velocities of:

i) NGP –14.54 ±1.06 km s^{-1}

ii) Vel –15.36 ±0.99 km s^{-1}

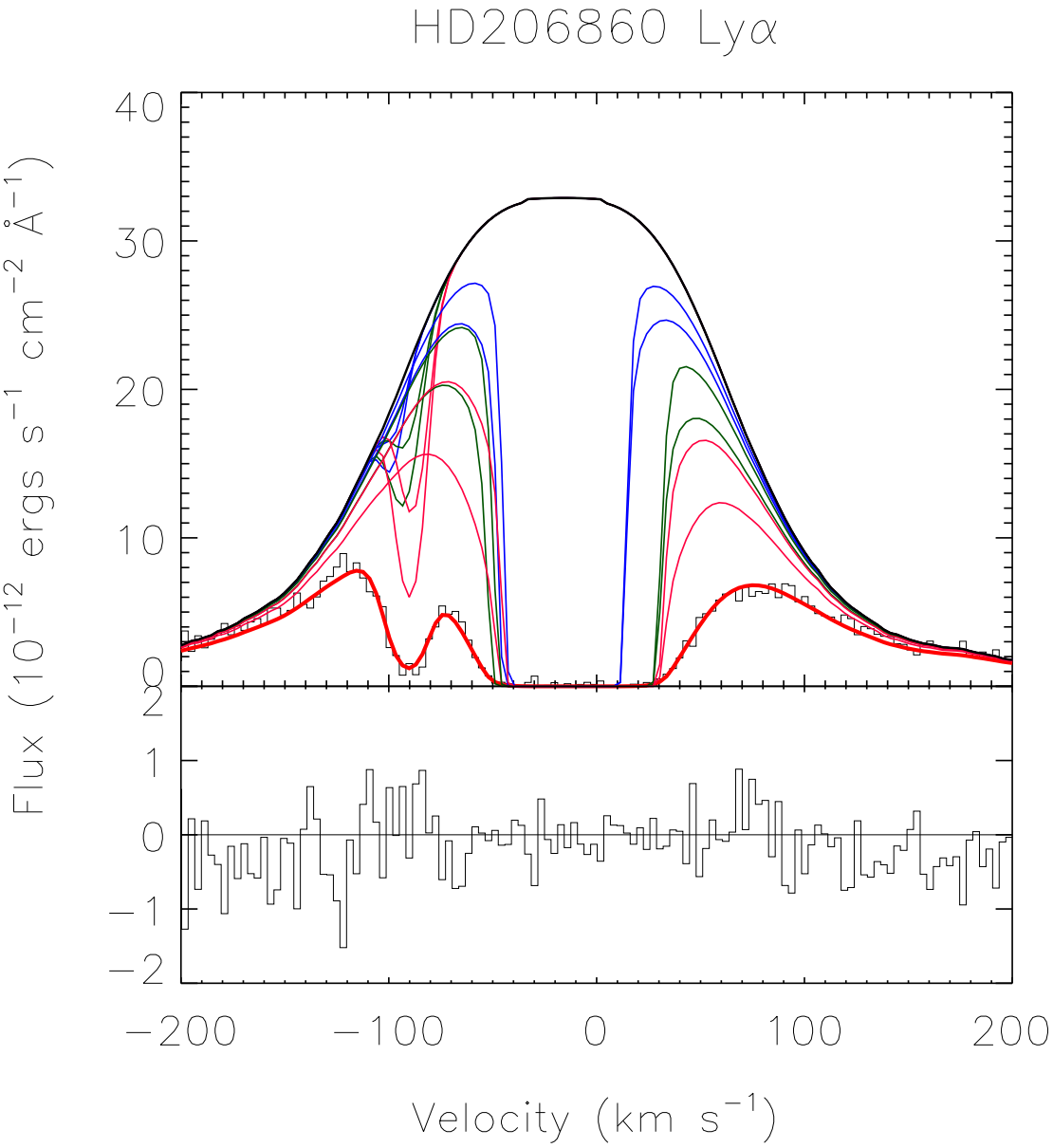

Figure 5.15: Same as Figure 5.1 for HD206860.

However, these clouds are not predicted to exist nearby this line of sight. Perhaps one of the clouds is extremely filamentary, and one of the filaments does intersect the line of sight, or perhaps the component does not belong to any

identifiable cloud.

5.5.1 Astrosphere/Heliosphere Detections

Unfortunately, there was no astrospheric or heliospheric absorption signal to be definitively uncovered from the Lyα line for HD206860, as exemplified by Figure 5.15. Unlike HD9826 and HD192310, the potential of an astrosphere will not be explored for this sight line.

Chapter 6

Applications

Now that the sight lines have been analyzed and all potential astrospheric and heliospheric absorption detections have been uncovered, what can actually be done with these results? The numbers discussed in Chapter 5 are not wind measurements, so now the task remains to apply the data to available models to obtain wind strength estimates. This chapter will outline the process thereof and discuss instances where modeling has been applied to sight lines in this data set.

6.1 Contextualizing Absorption Detections

The two important ingredients to consider at the astrospheric boundary are the hot, energetic stellar plasma and the comparably sluggish neutral hydrogen from the ISM. When atoms from these two populations meet, charge exchange can occur, with the neutral HI from the ISM giving an electron to the proton associated with the stellar wind (Gayley et al. 2003). This creates a population of pickup protons, which are ionized ISM protons that are 'picked up' and accelerated by the solar wind after charge exchange occurs (Luhmann 1997), and very hot neutral hydrogen at the heliospheric boundary that can be measured as, when compared with ISM Lyα, extremely broad, redshifted heliospheric or blueshifted astrospheric absorption.

Chapter 3 introduced the concept of Doppler broadening, which can be used to

explain why astrospheric Lyα would be an extremely wide feature. The Doppler width is strongly associated with the temperature of the emitting or absorbing population. For example, the first astrospheric measurement from Linsky & Wood (1996), had a b value estimate of 21.9 km s^{-1}, while the ISM Lyα had a b value of 11.8 km s^{-1}, which translates to a temperature of 30,000 K and 8,000 K respectively. While the 8,000 K measurement is a temperature typical for warm ISM, the 30,000 K is over and above what the local ISM population could provide (Wood et al. 2004).

The high blueshift of the astrospheric absorption and the redshift of the heliospheric feature have to do with *HST* being outside of the astrosphere and inside of the heliosphere. The energetic plasma neutrals from the observed star are speeding towards the Sun, while the hot solar HI that *HST* observes is moving out and away. This is a simplified explanation of an issue that involves some complex magnetohydrodynamic (MHD) physics, but essentially boils down to a question of rest frame (Wood et al. 2004).

6.1.1 The Importance of the ISM

As can be gleaned from Section 6.1, the ISM plays an essential role in the formation of a hot, neutral HI population at the astrospheric boundary. Particularly, the star must be surrounded by neutral ISM in order for the charge exchange that forms the backbone of the detectable Lyα emission to occur. This means that even if solar-like stars have extremely strong winds, if they are surrounded by completely ionized ISM, the detection method for astrospheres considered in this thesis would be ineffective.

6.2 Comparing Results to the Models

When considering how to translate astrospheric absorption measurements into stellar wind measurements, it is first important to start with the strongest consistent flow of information available: the Sun. *Voyager 1* and *Voyager 2* have both crossed the termination shock in 2004 and 2007 respectively (Zank et al. 2009), and so there have been direct measurements of the structure of the heliosphere, as described in Chapter 1, for at least a decade now. From these two spacecraft in situ quantities such as plasma pressures and magnetic field strength at different points within the heliosphere have been acquired (Decker et al. 2008).

Through information delivered from the *Voyagers* alongside other solar physics telescopes such as *SOHO* and *Ulysses*, astronomers have been able to develop MHD and kinematic models of the heliosphere that focus on the interaction between the solar plasma and the ISM neutrals. These models can then be applied to stellar systems of solar analogs by changing a few essential system variables.

First, in order to model the stellar wind of a particular star, the ISM flow vector relative to that star needs to be defined. When considering interactions between the ISM neutral and stellar plasma, the speed and direction of the incoming ISM is an important parameter to consider. This vector helps constrain the orientation of the nose of the heliosphere in 3-D space (Wood et al. 2004).

Another important property to consider is the HI density of the cloud surrounding the star. How different is the ionization fraction of hydrogen in that cloud relative to the local interstellar cloud (LIC) which surrounds the Sun? For most astrospheric modeling projects, the known LIC ionization fraction and density has been used, because, for nearby stars, which tend to be the ones targeted for astrospheric measurements, the differences between clouds are thought to be

marginal and unlikely to largely effect the output model (Wood et al. 2004).

Once the properties of the ISM have been determined, numerous models of the astrosphere can be computed that simulate different mass loss rate (or stellar wind strength) scenarios for the star. A good initial guess for the mass loss rates comes from the star's X-ray flux. Both the X-ray flux and mass loss of solar-like stars heavily involve the star's coronal activity (Wood et al. 2005), and a proportionality relationship has been derived, as shown in Figure 6.1.

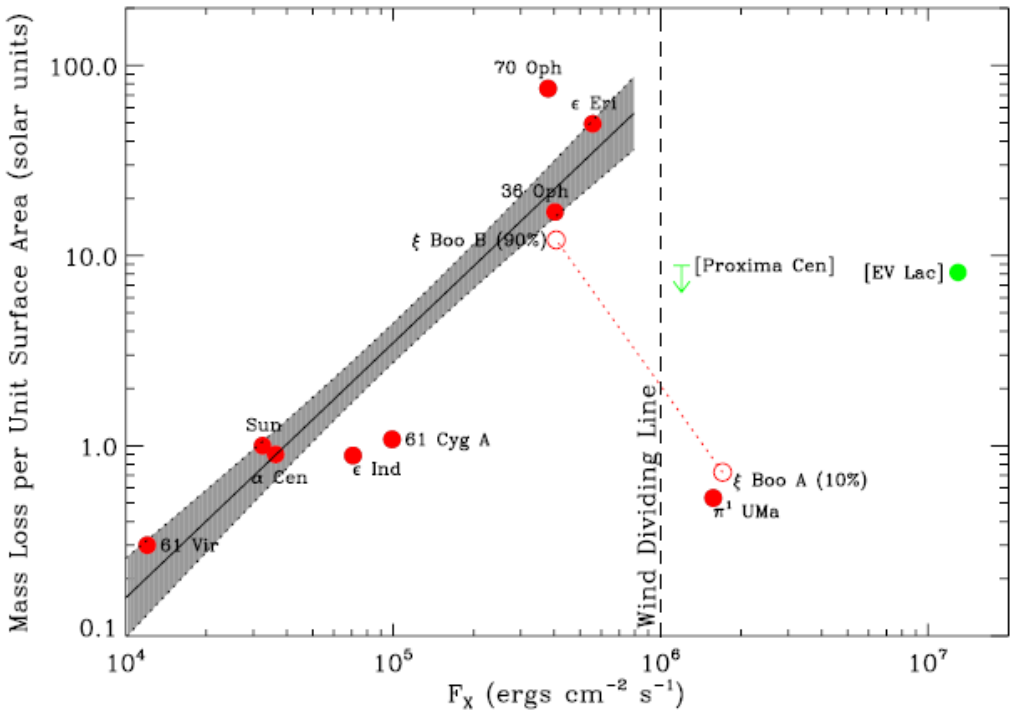

Figure 6.1: The relationship between stellar X-ray flux (F_x) and mass loss rates ($\dot{M}$) for solar-like stars from Wood et al. (2014b). The proportionality between the two quantities goes as $\dot{M} \propto F_x^{1.34\pm0.18}$ until F_x gets as large as 10^6 ergs cm^{-2} s^{-1}, where the relationship appears to change dramatically, as $\dot{M}$ sharply decreases for a given F_x.

Using this relationship as a starting point, reasonable mass loss rates for a given X-ray flux can be modeled. These models will produce hypothetical astrospheric absorption features, which can be reinserted into the Lyα profile for the line of sight to test the feasibility of the results. Figure 6.2 shows six examples of this

tactic. Out of the various mass loss rates modeled, the one that best reproduces the absorption seen along the Lyα line can be considered the most reasonable fit Wood et al. (2004).

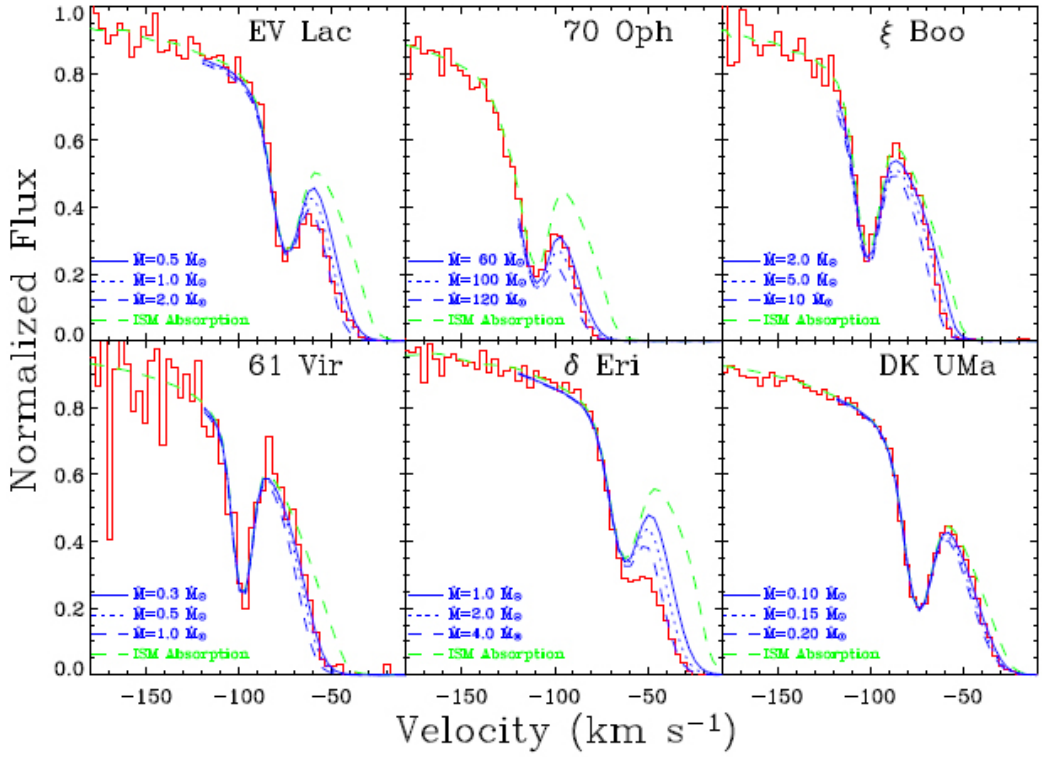

Figure 6.2: Wood et al. (2005) provide the results of astrospheric modeling for six nearby stars. The plots show the extremely blueshifted regime of the HI Lyα line, with the DI dip clearly visible. Different mass loss rate models are plotted on the figures to determine and demonstrate the feasibility of each.

With this technique, mass loss rates can be estimated from astrospheric measurements! However, because the present models used to produce potential astrospheres are very much a work in progress, there is a bit of uncertainty associated with the derived measurements. The mass loss rates measured from this technique are expected to have associated errors approximately of a factor of 2 (Wood et al. 2002). Even so, this way of estimating stellar wind strengths for solar-like stars is

the most sensitive technique presently available, and detection for eight solar-like stars have been achieved (Wood et al. 2014b).

6.3 Winds Versus Exoplanetary Atmospheres

One question to ask, however, is why it is important to know the strength of the winds of solar-like stars? What relevance do they carry to astronomical studies of the universe?

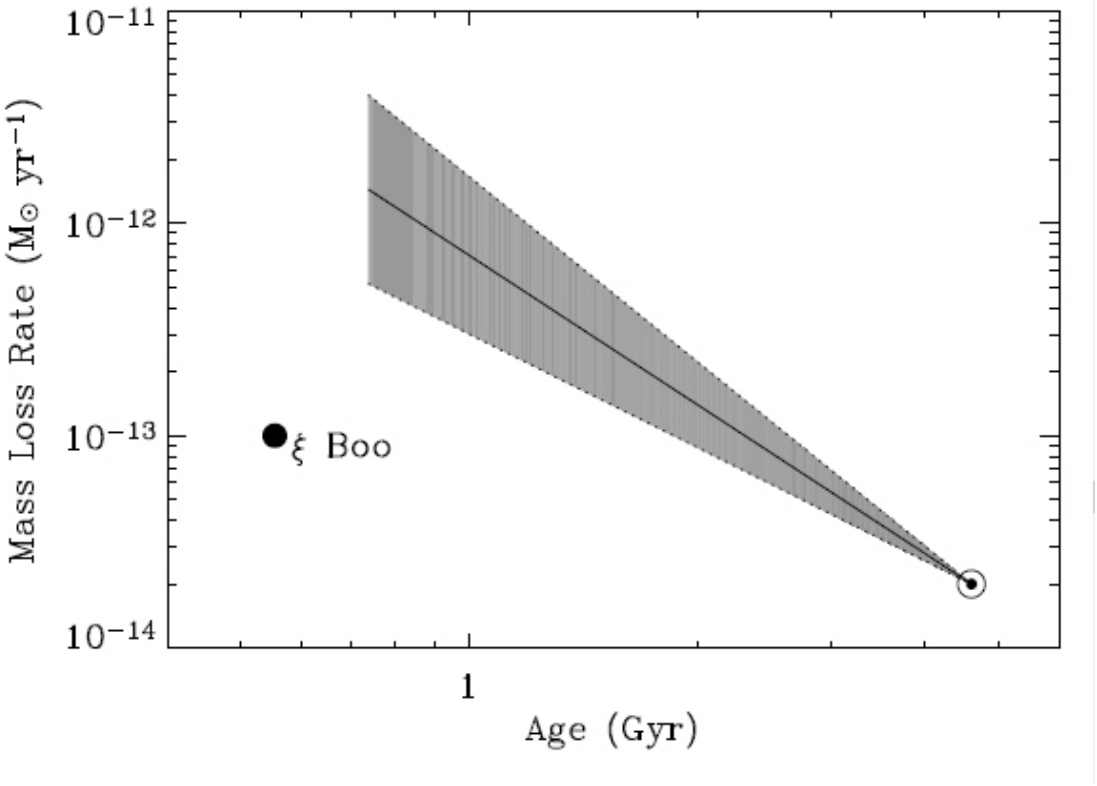

Figure 6.3: The age of the Sun in gigayears versus mass loss rate, with the present solar mass loss rate acting as the normalization constant. The younger the Sun, the higher the estimated mass loss rate, until the relationship appears to break down around at approximately 0.7 gigayears. The figure is from Wood et al. (2002)

One particularly important application is the investigation of winds in terms of exoplanetary habitability. There is evidence that Mars used to have a much

more robust atmosphere than it now does, and one possible factor as to why it lost its atmosphere 4 billion years ago could be the winds of an active, younger Sun (Wood et al. 2004). Figure 6.3 shows the solar age versus wind strength predicted relation as it now stands. As more stellar wind estimates are obtained for solar-like stars, the relationship between wind strength and age can be more conclusively defined, which could supply the answer as to whether the Sun could have reasonably contributed to Mars' atmospheric loss at the time.

Mars' atmospheric loss serves as a potential example for what could happen to unfortunate exoplanets in other stellar systems. If a solar-like star is a certain age, how close to the star is too close in terms of potential danger zones for atmospheric loss? When investigating the habitability of distant planets, the influence of winds on the system in question would be important to consider. If a planet further than the orbit of Earth could hypothetically be negatively influenced by the winds of a solar-like host star, this could mean that planets within the habitable zones of solar-like stars could very well experience atmospheric loss of a magnitude catastrophic for life.

More measurements of solar-like stellar winds will help to constrain the wind strength evolution of these stars, and make it easier to consider the effects of these winds on their host planets.

6.4 Data Set Modeling

In this data set there was one successful detection of an astrosphere, which will be considered here. Also, while HD9826 and HD192310 experienced non-detections, hypothetical detections for these two systems will be considered.

6.4.1 HD72905

This astrospheric detection was particularly fortuitous, because of the youthful age of the solar-like star under consideration. As discussed in Section 6.3, the evolution of solar-like wind with age is an important relationship to consider in terms of exoplanetary atmospheric loss and habitability in other systems. HD72905 is a G-type 500 million year old star, so it can be considered very young relative to the Sun and extremely solar-like in its spectral class. A measurement of this stars stellar winds provides an informative data point for this important solar-like age versus mass loss rate relationship.

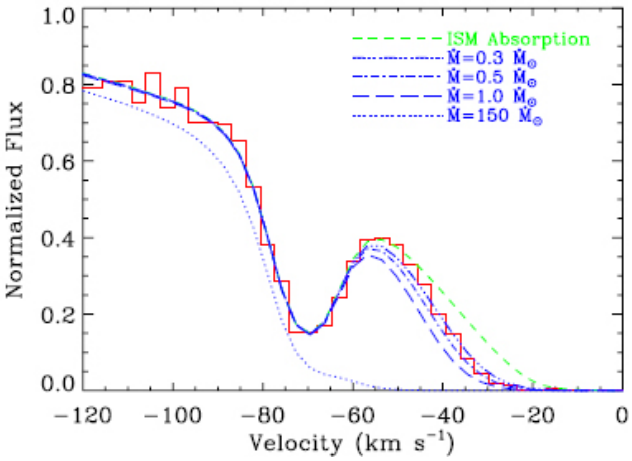

Figure 6.4: Same as Figure 6.2 for HD72905 from Wood et al. (2014b).

The results of the modeling by Wood et al. (2014b) are shown in Figure 6.4. The best fit for this model ended up being a mass loss rate of .5 $\dot{M}_{\odot}$. If this star were to follow the $\dot{M} \propto F_x^{1.34\pm0.18}$, as a young, active star it would be expected to have a mass loss rate of 150 $\dot{M}_{\odot}$ (Wood et al. 2014b)! This is a huge discrepancy that must be addressed. Does this mean that there is a break in the flux versus mass loss relationship at high flux values, as Figure 6.1 hinted? Or is there an issue with the value derived from this detection method?

If the value is correct, this measurement provides support for the Sun having weaker winds in its youthful, more active past. This would not necessarily mean that the Sun had weaker winds for all of its youth. Perhaps there were epochs of strong and weak winds littered throughout the solar history. In any case, more solar-like stellar wind estimates of stars at different ages are needed to put significant constraints on this history. The possibility of solar winds causing Mars' atmospheric erosion has not become an impossibility just yet.

However, there is also the chance that this stellar wind measurement is inaccurate, which could be due to various uncertainties associated with this detection method. For example, if HI densities and ionization fraction associated with the ISM surrounding HD72905 are entirely unlike the LIC parameters derived for the heliosphere, the model created for this circumstance could be extremely unlike the actual astrosphere surrounding the star (Wood et al. 2014b). However, considering how close the star is, at a distance of 14.36 parsecs, seeing an extreme variation in the ISM in that area seems unlikely.

All signs point towards a likely detection. However, a larger sample size will be the most important factor in determining whether this stellar wind measurement is appropriate.

6.4.2 HD9826 and HD192310

The lines of sight toward HD9826 and HD192310 were chosen particularly because the stellar systems have confirmed exoplanets in orbit. If astrospheric absorption had been detected within either or both sight lines, it would have been a great opportunity to compare the absorption to models, with a mass loss rate gleaned through comparing the models to the absorption feature and discerning

the fit, as was done in Section 6.4.1 with HD72905. With a measured mass loss rate, these systems could be investigated in terms of how the known planets in the systems might have been affected by the stellar outflow.

However, in this case, as discussed in Chapter 5, no astrospheric signals were found for either HD9826 or HD192310. There are many possible reasons for a non detection, such as the ISM signal oversaturating the Lyα line so that no astrospheric absorption could be discerned. This does not necessarily mean that there is no astrosphere to be found around the star, which means that it can be a fruitful exercise to model what a hypothetical astrosphere would be, based on past measurements of the heliosphere and other nearby astrospheres.

Using the X-ray fluxes of these stars as a way to estimate the mass loss rate, and using the properties of the LIC as stand ins for the ISM properties near the stars under consideration, Hans Müller created models of the hypothetical solar-like astrospheres surrounding both stars, as shown by Figure 6.5.

The significant feature to note is the neutral HI wall, shown in red, white, and purple, where the hot neutral HI is densest, surrounding the nose of the astrosphere. This is the HI that is detected in the Lyα spectral feature as an astrospheric absorption detection at high blueshift. Figure 6.5a and 6.5b show that the line of sight to these stars clearly goes through a significant portion of the HI wall, so the non-detection cannot be attributed to a poor line of sight, as long as the LIC velocity vector used to calculate these models was a reasonable approximation for the LISM conditions for each star.

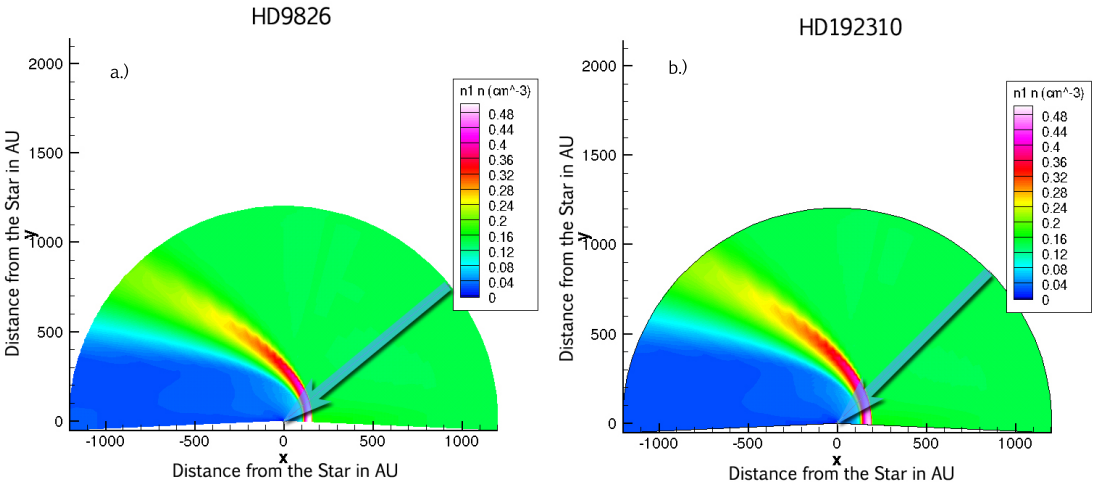

Figure 6.5: Models provided by Hans Müller for the hot neutral H1 density distribution surrounding the stars, with each respective star positioned where x and y equal 0. a) shows the H1 density for HD9826, with the line of sight at 39.6° signified by the blue arrow. b) shows the same but for HD192310, with the line of sight at an angle of 44.7°.

If the nose of the astrosphere is, in reality, positioned at angle in relation to the solar system that would only allow *HST* to observe the star through the dark blue region, an astrospheric absorption detection through the Lyα method would be highly unlikely, because of the lack of hot, neutral HI to provide absorption. More constraints on the LISM near these stars, as well as more astrospheric detections in general would help to further parse the reasons for the non-detections.

Chapter 7

Conclusions and Future Work

Detecting stellar winds of solar-like stars is a fledgling field that has many incredibly useful applications for studying nearby stellar systems, as well as our own solar system. However, as the situation currently stands in the astronomical community, we are working with a detection method with an impending expiration date. As old telescopes fade and orbitally degrade into obscurity, will new relevant instruments and stellar wind detection techniques rise to take their place? Only time and measured interest will tell.

7.1 The Last of *Hubble*

With the end of the shuttle program, there is no longer a way to service the *HST*, which spells out an eventual inevitable end for the telescope. The *HST* is orbiting the Earth in the thermosphere, which is close enough for its orbit to continually, slowly degrade. With each servicing mission in the past, the orbital degradation was corrected for by pushing the telescope higher in the atmosphere. Now, without the occasional servicing mission, there will be no way to correct for the orbital decay. Without further interference and if no other extraneous issues affect the functionality of its systems before then, the telescope is predicted to

undergo reentry in the year 2040 ±10.[1]

This is certainly bad news, and it gets worse. With *Hubble's* demise, there will be no instruments available with the precision and wavelength range to detect Lyα absorption and, by proxy, stellar winds. Without *HST* in action, there will effectively be no option to measure any more stellar winds of solar-like stars (Wood et al. 2014b).

7.1.1 Options to Consider

For now, while *HST* is still taking data, it is important to take observations with STIS towards as many viable, nearby stellar candidates for this detection method as possible. This means sending in *Hubble* proposals for observations of these stars in the Lyα wavelength to gather up a good sample size of solar-like astrospheres before this possibility is no longer available. There are presently detections of astrospheres towards 9 different solar-like stars (Wood et al. 2014b), including the one detection in this data set, and an increase in this number would provide further constraints on the solar-like stellar wind evolution.

There is also the possibility of finding viable *Hubble* data to analyze in the *HST* archive. Sometimes *Hubble* proposals that do not directly involve stellar wind measurements still include the wavelength range towards ideal stars for this technique. Even if the data is towards stars where astrospheric absorption measurements have been obtained before, it can still be a good idea to take a look at the system if new spectral measurements are available. A second analysis can provide important information on how an astrosphere might change with time, as

[1] *An Early Study of Disposal Options for the Hubble Space Telescope*, which provides the reentry estimation cited here, was a presentation by NASA Goddard employees at the 2013 International Association for the Advancement of Space Safety (IAASS) conference. It can be found under Session 32 at: `http://iaassconference2013.space-safety.org/presentations-available/`

well as provide a resource to compare the reasonableness of both fits of the same Lyα line.

Wood et al. (2005) searched the archive for reasonable data and were able to detect 7 new astrospheres from their endeavors. Data will continue to be added to the archive until the end of the *HST* mission, so there are likely to be years of more archival data to search through before the telescope's end.

7.2 The Beginnings of *James Webb*

Carrying the prized moniker of successor to *HST*, the *James Webb Space Telescope* (*JWST*) is planned to launch in 2018 (Tiscareno et al. 2014), and will bring along with it many exciting, higher-than-ever-before resolution ways to dissect the universe. While it will not encompass the Lyα wavelength regime, the instruments aboard this next generation space telescope still have the potential to be extremely helpful on the hunt for stellar wind and exoplanetary atmospheric interaction.

7.2.1 Options to Consider

JWST has four main science goals. One of which is known as "The Planetary Systems and Origins of Life," (Sonneborn 2008) which follows the spirit, if not identity, of this thesis's stellar wind hunt. The aim is to characterize exoplanetary systems physically and chemically in order to analyze habitability potential (Sonneborn 2008).

Where this thesis focuses more on the stellar wind half of the stellar wind-exoplanetary atmosphere relationship, the *JWST* will focus its instruments on the other half. Two instruments aboard *JWST*, NIRCam and NIRSpec, will meld

spectroscopy with exoplantary transits. For example, by looking at the light transmitted through an exoplanet's atmosphere during transit with *JWST*, the atmosphere's absorption spectrum can be classified by determining what parts of the stellar spectrum are absorbed by the atmosphere when the planet is transiting in front of the star (Clampin 2010).

A strong understanding of the atmospheric characteristics of the various types of exoplanets at different distances from host stars of different stellar types may provide some indirect evidence of stellar wind influence. Perhaps trends may emerge, such as a discovery that terrestrial planets of solar-like stellar systems inwards of a certain distance to their host star will be found unlikely to host reasonable atmospheres.

Whatever results come to the fore from *JWST* exoplanetary atmospheric studies, they are sure to provide ample room to speculate about the influence that the winds of the host stars may have had upon the studied systems. It is my hope that the speculation may lead to an interest in further measurement and classification of these winds - interest that could put the wheels in motion for a new space project with instrumentation that supports the Lyman regime. For now, however, it is important to take advantage of the wealth of information the Lyα line holds while it is still around to be got.

Bibliography

Ayres, T. R. 2010, VizieR Online Data Catalog, 218, 70149

Ayres, T. R., et al. 1995, ApJS, 96, 223

Ben-Jaffel, L., Strumik, M., Ratkiewicz, R., & Grygorczuk, J. 2013, ApJ, 779, 130

Clampin, M. 2010, in Astronomical Society of the Pacific Conference Series, Vol. 430, Pathways Towards Habitable Planets, ed. V. Coudé du Foresto, D. M. Gelino, & I. Ribas, 167

Crawford, I. A. 2011, Acta Astronautica, 68, 691

Decker, R. B., Krimigis, S. M., Roelof, E. C., Hill, M. E., Armstrong, T. P., Gloeckler, G., Hamilton, D. C., & Lanzerotti, L. J. 2008, Nature, 454, 67

Echim, M. M., Lemaire, J., & Lie-Svendsen, Ø. 2011, Surveys in Geophysics, 32, 1

ESA. 2008, Solar Winds Measured By Ulysses

Feldman, U., Landi, E., & Schwadron, N. A. 2005, Journal of Geophysical Research (Space Physics), 110, 7109

Forsyth, B., & Breen, A. 2002, Astronomy and Geophysics, 43, 3.32

Gayley, K. G., Zank, G. P., Pauls, H. L., Frisch, P. C., & Welty, D. E. 2003, ApJ, 592, 1241

Gurnett, D. A., Kurth, W. S., Burlaga, L. F., & Ness, N. F. 2013, Nature, 341, 1489

Hernandez, S., e. a. 2011, "STIS Instrument Handbook," Version 13.0, (Baltimore: STScI)

Hilborn, R. C. 2002, ArXiv Physics e-prints

Izmodenov, V. V. 2002, ArXiv Astrophysics e-prints

Jenkins, E. B. 2014, ArXiv e-prints

Lamers, H. J., & Cassinelli, J. P. 1999, Introduction to Stellar Winds (Cambridge, UK: Cambridge University Press)

Leitherer, C., Chapman, J. M., & Koribalski, B. 1997, ApJ, 481, 898

Lemieux, C. 2009, Monte Carlo and Quasi-Monte Carlo Sampling (Springer New York)

Linsky, J. L. 1998, Space Science Reviews, 84, 285

Linsky, J. L., & Wood, B. E. 1996, ApJ, 463, 254

Linsky, J. L., Wood, B. E., & Zank, G. P. 2003, in Measurements of the winds of solar-like stars and their influence on extrasolar planets, 507–511

Luhmann, J. G. 1997, ApJ, 487, 259

McComas, D. J., et al. 2012, Science, 336, 1291

Michelson, A. A. 1898, ApJ, 8, 37

Morton, D. C. 2004, ApJS, 151, 403

Müller, H.-R., Florinski, V., Heerikhuisen, J., Izmodenov, V. V., Scherer, K., Alexashov, D., & Fahr, H.-J. 2008, AAP, 491, 43

Opher, M., Stone, E. C., & Liewer, P. C. 2006, ApJL, 640, L71

Porter, M. J. 2000, Astrophysics and Space Science, 273, 217

Quinten, M. 2012, A Practical Guide to Optical Metrology for Thin Films (Wiley-VCH Verlag GmbH Co. KGaA)

Redfield, S., & Linsky, J. L. 2001, ApJ, 551, 413

Redfield, S., & Linsky, J. L. 2002, ApJS, 139, 439

Redfield, S., & Linsky, J. L. 2004a, ApJ, 602, 776

Redfield, S., & Linsky, J. L. 2004b, ApJ, 613, 1004

Redfield, S., & Linsky, J. L. 2008, ApJ, 673, 283

Scherer, K., & Fichtner, H. 2014, ApJ, 782, 25

Simpson, J., ed. 2013, Oxford English Dictionary (Oxford University Press)

Sonneborn, G. 2008, in Clumping in Hot-Star Winds, ed. W.-R. Hamann, A. Feldmeier, & L. M. Oskinova, 229

Taylor, J. R. 1997, An Introduction to Error Analysis (University Science Books)

Tiscareno, M. S., et al. 2014, ArXiv e-prints

Wolszczan, D. A., & Frail, D. A. 1992, Nature, 355, 145

Wood, B. E., Ambruster, C. W., Brown, A., & Linsky, J. L. 2000, ApJ, 542, 411

Wood, B. E., Izmodenov, V. V., Alexashov, D. B., Redfield, S., & Edelman, E. 2014a, ApJ, 780, 108

Wood, B. E., Mller, H. R., Zank, G. P., Izmodenov, V. V., & Linsky, J. L. 2004, Advances in Space Research, 34, 66

Wood, B. E., Müller, H.-R., Redfield, S., & Edelman, E. 2014b, ApJL, 781, L33

Wood, B. E., Müller, H.-R., Zank, G. P., & Linsky, J. L. 2002, ApJ, 574, 412

Wood, B. E., Müller, H.-R., Zank, G. P., Linsky, J. L., & Redfield, S. 2005, ApJ Letters, 628, L143

Zank, G. P., Pogorelov, N. V., Heerikhuisen, J., Washimi, H., Florinski, V., Borovikov, S., Kryukov, I., & Müller, H. R. 2009, SSR